

# We are IntechOpen, the world's leading publisher of Open Access books Built by scientists, for scientists

6,900

Open access books available

186,000

International authors and editors

200M

Downloads

Our authors are among the

154

Countries delivered to

TOP 1%

most cited scientists

12.2%

Contributors from top 500 universities



WEB OF SCIENCE™

Selection of our books indexed in the Book Citation Index  
in Web of Science™ Core Collection (BKCI)

Interested in publishing with us?  
Contact [book.department@intechopen.com](mailto:book.department@intechopen.com)

Numbers displayed above are based on latest data collected.  
For more information visit [www.intechopen.com](http://www.intechopen.com)



# Ultra-Broadband Time-Resolved Coherent Anti-Stokes Raman Scattering Spectroscopy and Microscopy with Photonic Crystal Fiber Generated Supercontinuum

Hanben Niu<sup>1,2</sup> and Jun Yin<sup>1,2</sup>

<sup>1</sup>College of Optoelectronic Engineering, Shenzhen University, Shenzhen

<sup>2</sup>Key Laboratory of Optoelectronic Devices and Systems of Ministry of Education and Guangdong Province, Shenzhen University, Shenzhen  
China

## 1. Introduction

Optics, one of the oldest natural sciences, has been promoting the developments of sciences and technologies, especially the life science. The invention of the optical microscope eventually led to the discovery and study of cells and thus the birth of cellular biology, which now plays a more and more important role in the biology, medicine and life science. The greatest advantage of optical microscopy in the cellular biology is its ability to identify the distribution of different cellular components and further to map the cellular structure and monitor the dynamic process in cells with high specific contrast. In 1960's, with the invention of laser, an ideal coherent light source with high intensity was provided. Since then the combination of optical microscopy with laser has been expanded. Many novel optical microscopic methods and techniques were developed, such as various kinds of fluorescence microscopy. In fluorescence microscopy, the necessary chemical specificity is provided by the labeling samples with extrinsic fluorescent probes [1, 2]. With the developments of ultra-short laser, fluorescent labeling technique and modern microscopic imaging technique, the fluorescence spectroscopy and microscopy with high spatial resolution, sensitivity and chemical specificity has become the key promotion of the life science and unveiled many of the secrets of living cells and biological tissues [3, 4]. In particular, the confocal fluorescent microscope (CFM), with the confocal detection [5] and multi-photon excitation [6, 7], can obtain the 3D sectioning images of cells and tissues with high spatial resolution. Today, fluorescence microscopy has become a powerful research tool in life science and has achieved the great triumph. Nevertheless, the disadvantages of fluorescence microscopy, such as the photo-toxicity and photo-bleaching, can not be ignored [8]. Furthermore, some molecules in cells, such as water molecule and other small biomolecules, can not be labeled until now. Finally, for the biological species that do not fluoresce, the extrinsic fluorescent labels will unavoidably disturb the original characteristics and functions of biological molecules, which will limit the applicability of fluorescence microscopy. Therefore, it is very necessary to develop some complementary

methods with molecular specificity, high spatial and temporal resolution, but without any extrinsic labels.

Now some imaging techniques without any extrinsic labels have been developed, such as the harmonic generation microscopy (second harmonic generation, SHG [9-13] and third harmonic generation, THG [14, 15]), infrared microscopy [16], Raman microscopy [17-19], Stimulated Raman Scattering (SRS) microscopy [20] and coherent anti-Stokes Raman scattering (CARS) microscopy [21, 22]. The specificity and contrast of SHG and THG imaging arise from the unique non-centrosymmetric structure of specific biological tissues, such as the collagen fibrils, microtubules and myosin, but the structural information can not be obtained at molecular level. Because of longer wavelength involved and vibrational absorption of the common solvent, the spatial resolution of infrared imaging technique is too low. With the Raman scattering spectrum, we can distinguish different molecules [17-19]. However, higher average power laser is necessary due to small Raman scattering cross-section and autofluorescence background that limit its applicability in life science. Both SRS and CARS are essentially Raman scattering, the molecules of a sample can be distinguished by their active vibrational modes of specific molecular bonds, which provide the necessary imaging contrasts and specificities [20-26]. As a coherent resonance-enhance process, the CARS signal is not only many orders higher than spontaneous Raman scattering signal but also well oriented in emission direction, which significantly reduce the integration time. The wavelength of CARS signals is blue-shift relative the excitation, the interference of strong one-photon fluorescence background can be avoided. Furthermore, as a nonlinear optical process, the CARS signals are generated in a small focal volume under the tight-focusing condition. Thus, the CARS microscopy can provide high temporal and spatial resolution, and strong 3D sectioning imaging ability. The information of molecular distributions of a biological sample can be obtained without any disturbance on sample.

In 1965, CARS was first reported by P. D. Maker and R. W. Terhune [27]. They found that a very strong signal could be obtained when two coherent light beams at frequencies  $\omega_1$  and  $\omega_2$  were used to drive an active vibrational Raman mode at frequency  $\Omega_R = \omega_1 - \omega_2$ . It was named as the CARS process, whose signals are  $10^5$  stronger than spontaneous Raman scattering process [28]. As a tool for spectral analysis, the CARS spectroscopy was extensively studied and used in physics and chemistry [29-32]. The first CARS microscopy with noncollinear beams geometry was demonstrated by M. D. Duncan et al in 1982 [21]. In 1999, A. Zumbusch and his colleagues revived the CARS microscopy by using an objective with high numerical aperture, collinear beams geometry and detection of CARS signals in forward direction that boosted wide research in the improvements of CARS microscopy [22]. The distinguished research works of Prof. S. Xie and his colleagues proved that the CARS microscopy was a very effective noninvasive optical microscopic approach with high spatial resolution and imaging speeds matching those of multi-photon fluorescence microscopy and had a great prospect in biology, medicine and life science [22, 33].

In a traditional CARS microscopy, the contrast and specificity are based on single or few chemical bonds of molecule due to the limitation of laser line-width. It is not adequate to distinguish various biological molecules with just single chemical bond. In order to effectively distinguish different molecules, a method for simultaneously obtaining the complete molecular vibrational spectra is required. For this purpose, many methods for extending the simultaneously detectable spectral range of CARS spectroscopy and

microscopy are presented [34-38]. With the advent and the progress of supercontinuum (SC) generated by photonic crystal Fibre (PCF) pumping with ultra-short laser pulses [39], the broadband CARS microscopy based on SC has been developed that provided better feasibilities [40-44].

As well known, CARS microscopy is not background-free [29]. Strong nonresonant background signals (NRB), from the electronic contributions to the third-order susceptibility of sample and the solvent, always company with the CARS signals in a broad spectral range. It often interferences or overwhelms CARS signals from small targets that limits the spectral accuracy, imaging contrast and systemic sensitivity. In the broadband CARS with a broadband pump source, it is not beneficial to simultaneously distinguish various biological molecules because of the influence of strong NRB.

In this chapter we briefly introduce the theoretical basics of the CARS process and characteristics of CARS spectroscopy and microscopy. The classical and quantum mechanical descriptions of Raman scattering and CARS processes are qualitatively reviewed in order to be helpful for understanding the physical mechanisms of these two light scattering processes. The main characteristics and applications of a CARS spectroscopy and microscopy are specifically emphasized, such as the condition of momentum conservation; the generation and suppression of NRB noise. In order to simultaneously obtain the complete molecular vibrational spectra, SC laser is a proper pump source. We will briefly review the history and characteristics of PCF. A summarization of the theoretical analysis of SC generation with PCF pumping by ultra-short (picosecond or femtosecond) laser pulses will be outlined. The necessities, developments and characteristics of the broadband CARS spectroscopy and microscopy will be briefly described. An ultra-broadband time-resolved CARS technique with SC generated by PCF will be especially emphasized. By this method, the complete molecular vibrational spectra without NRB noise can be obtained. During recent years, the ways to improve spatial resolution of CARS microscopy have become one of attractive questions all over the world. We will briefly review and outlook the feasible ways.

## 2. Theories of CARS process

As a coherent Raman scattering process, CARS is a typical three-order nonlinear optical process. In order to well understand the mechanism of the CARS process, the brief classical and quantum mechanical discussions of Raman scattering are necessary. Based on the theoretical analysis of Raman scattering, a theoretical description of the CARS process and the conditions for the generation of CARS signals will be outlined. The general classical description will give an intuitive picture. And the quantum mechanical description will enable the quantitative analysis of the CARS process. Here, we just carry out the qualitatively theoretical analysis, and the descriptions of physical mechanism will be highlighted. The emphases are the main characteristics of a CARS microscopy, such as the conditions for generation of CARS signals, and generation and suppression of NRB noise.

### 2.1 Raman scattering process

When a beam of light passes through a media, one can observe light scattering phenomenon besides light transmission and absorption. Most of elastically scattered photons (so called

Rayleigh scattering) from atom or molecule have the same energy (frequency) as the incident photons, as shown in figure 1 (a). However, a small part of the photons (approximately 1 in 10 million photons) are inelastically scattered with the frequencies different from the incident photons [45]. This inelastic scattering of light was theoretical predicted by A. Smekal in 1923 [46]. In 1928, Indian physicist Sir C. V. Raman first discovered this phenomenon when a monochromatic light with frequency of  $\omega_P$  was incident into a medium. He found that the scattered light components contained not only Rayleigh scattering with frequency of  $\omega_P$ , but also some weaker scattering components with frequencies of  $\omega_P \pm \Omega_R$ , which come from the inelastic scattering phenomenon of light named as Raman scattering or Raman effect [47, 48], as shown in figure 1 (b) and (c) in energy level diagram. Raman scattering originates from the inherent features of molecular vibration and rotation of individual or groups of chemical bonds. The obtained Raman spectra contain the inherent molecular structural information of the medium and can be used to identify molecules. Because of this significant feature, it has been widely used as a tool for analyzing the composition of liquids, gases, and solids.

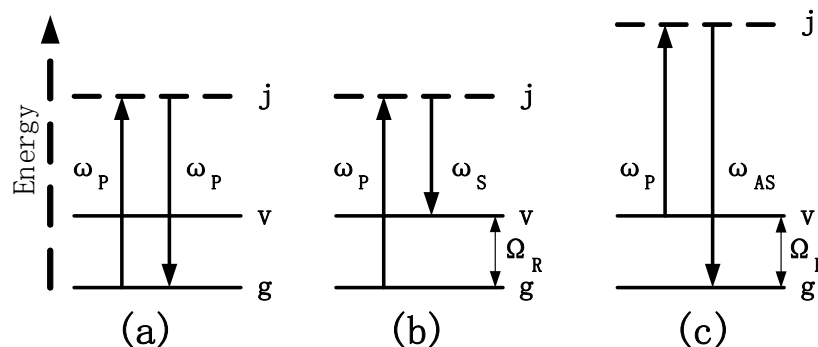


Fig. 1. Energy level diagram of the elastic Rayleigh scattering (a), the inelastic Stokes Raman scattering (b) and anti-Stokes Raman scattering (c), where  $\omega_P$ ,  $\omega_S$ ,  $\omega_{AS}$  and  $\Omega_R$  represents the frequency of incident light, Stokes scattering light, anti-Stokes scattering light and resonance respectively. The ground state level, the vibrational level and the virtual intermediate level is labeled with  $g$ ,  $v$ , and  $j$  respectively.

### 2.1.1 Classical description of raman scattering

The Raman scattering phenomenon arises from the interactions between the incident photon and the electric dipole of molecules. In classical terms, the interaction can be viewed as fluctuation of the molecule under the influence of the applied optical field. With the used optical field of frequency  $\omega_P$  expressed as  $E(t) = E(r)e^{-i\omega_P t}$ , the induced dipole moment of a molecule is:

$$\mu(t) = \alpha(t)E(t), \quad (2.1)$$

where  $\alpha(t)$  is the polarizability of the material. When the incident optical field interacts with the molecules, the polarizability can be expressed as a function of the nuclear coordinate  $Q$ , and expanded to the first order in a Taylor series [49]:

$$\alpha(t) = \alpha_0 + \frac{\partial \alpha}{\partial Q} Q(t), \quad (2.2)$$

where  $Q(t)$  is a simple harmonic oscillator,  $Q(t)=2Q_0\cos(\omega_R t)$ . So the induced dipole moment can be rewritten as:

$$\mu(t) = \alpha_0 E(r) e^{-i\omega_p t} + \frac{\partial \alpha}{\partial Q} E(r) Q_0 e^{\pm i(\omega_p \pm \Omega_R)t} . \quad (2.3)$$

On the right-hand side of equation (2.3), the first term corresponds to Rayleigh scattering with the same frequency of incident light. The second term describes the Raman frequency shift of  $\omega_p \pm \Omega_R$ . Because the Raman frequency shifting term depends on  $\partial \alpha / \partial Q$ , Raman scattering occurs only when the incident optical field induces a polarizability change along the specific molecular vibrational mode. This specific mode is an active Raman mode, which is the basis of the selection rule of Raman spectroscopy.

The differential scattering cross-section is one of key parameters to express the intensity of Raman scattering signal. In a solid angle  $\Delta\Omega$ , it can be defined as the amount of scattered intensity divided by the incident intensity:

$$\sigma_{diff} = \frac{\partial \sigma}{\partial \Omega} = \frac{I_{Raman}}{VNI_p \Delta\Omega} , \quad (2.4)$$

where  $I_{Raman}$  is the intensity of Raman scattering light in  $\Delta\Omega$ ,  $V$  is the volume of scattering medium,  $N$  is the molecular density,  $I_p$  is the intensity of incident optical field. Therefore, the total intensity of the Raman scattering light in whole solid angle can be described as the summation of contributions from all  $N$  molecules:

$$I_{Raman} = NI_p \int \sigma_{diff} d\Omega . \quad (2.5)$$

Obviously, the spontaneous Raman is a linear optical process, because the intensity of scattering signal has the linear relationship with the intensity of incident optical field and number of scattering molecules respectively. The classical description of Raman process only provides a qualitative relationship between the Raman scattering cross-section and intensities of the Raman signals. In order to achieve the quantitative study for the Raman process, a quantum mechanical description is necessary.

### 2.1.2 Quantum mechanical description of raman scattering

When the interaction between incident optical field and medium is studied with quantum mechanical method, the molecular system of medium should be quantized. The Raman scattering is a second-order process in which two interaction processes between incident optical field and medium are involved. The quantum mechanical explanation of the Raman scattering process is based on the estimation of the transition rate between the different molecular states. In quantum physics, the Fermi's golden rule is a common way to calculate the first-order transition rate between an initial state  $|g\rangle$  and a final state  $|v\rangle$  that is proportional to the square modulus of the transition dipole  $\mu_{vg}$ . But in order to describe the Raman process, we need to calculate the second-order transition rate. The second-order transition rate  $\tau^{-1}$  can be presented as [50, 51]:

$$\frac{1}{\tau} = \sum_{\nu} \sum_{R} \frac{\pi e^4 \omega_P \omega_R n_R}{2 \epsilon_0^2 \hbar^2 V^2} \left| \sum_j \left\{ \frac{\mu_{\nu j} \mu_{jg}}{\omega_j - \omega_P} + \frac{\mu_{\nu j} \mu_{jg}}{\omega_j + \omega_R} \right\} \right|^2 \delta(\omega_{\nu} + \omega_R - \omega_P), \quad (2.6)$$

where  $e$  is the electron charge,  $\epsilon_0$  is the vacuum permittivity,  $\hbar$  is Planck's constant,  $n_R$  is the refractive index at Raman frequency, and  $\delta$  is the Dirac delta function.  $\omega_P$  is the frequency of incident optical field and  $\omega_R$  is the frequency of Raman scattering light. The frequencies  $\omega_{\nu}$  and  $\omega_j$  are the transition frequencies from the ground state to the final state  $|\nu\rangle$  and intermediate state  $|j\rangle$ , respectively.

In Raman scattering process, an incident optical field first converts the material system from the ground state  $|g\rangle$  to an intermediate state  $|j\rangle$ , which is an artificial virtual state. Then, the transition from the intermediate state  $|j\rangle$  to the final state  $|\nu\rangle$  happens that is considered as an instantaneous process. A full description of Raman scattering thus incorporates a quantized field theory [52]. From the quantized field theory, we can find the number of photon modes at frequency of  $\omega_R$  in volume of medium  $V$  [52], and perform the summation over  $R$  in equation (2.6). From the argument of the Dirac delta function, the only nonzero contributions are the ones for which the emission frequency  $\omega_R = \omega_P - \omega_{\nu}$ , the red-shifted Stokes frequencies. With  $\sigma_{diff} = d/d\Omega(V/cn_R\tau)$ , the expression for the transition rate can be directly presented with the differential scattering cross-section [51]:

$$\sigma_{diff} = \sum_{\nu} \frac{e^4 \omega_P \omega_R^3}{16\pi^2 \epsilon_0^2 \hbar^2 c^4} \left| \sum_j \left\{ \frac{\mu_{\nu j} \mu_{jg}}{\omega_j - \omega_P} + \frac{\mu_{\nu j} \mu_{jg}}{\omega_j + \omega_R} \right\} \right|^2. \quad (2.7)$$

This is the Kramers-Heisenberg formula, which is very important in quantum mechanical description of light scattering [50]. For Raman scattering process, the differential scattering cross-section for a particular vibrational state  $|\nu\rangle$  can be simplified to:

$$\sigma_{diff} = \frac{\omega_P \omega_R^3}{16\pi \epsilon_0^2 \hbar^2 c^4} |\alpha_R|^2, \quad (2.8)$$

where the Raman transition polarizability  $\alpha_R$  can be written as:

$$\alpha_R = \sum_j \left\{ \frac{\mu_{\nu j} \mu_{jg}}{\omega_j - \omega_P} + \frac{\mu_{\nu j} \mu_{jg}}{\omega_j + \omega_R} \right\}. \quad (2.9)$$

From the above discussion, we can know that Spontaneous Raman scattering is a weak effect because the spontaneous interaction through the vacuum field occurs only rarely. Although Raman scattering is a second-order process, the intensity of Raman signal depends linearly on the intensity of the incident optical field. When the frequency approaches the frequency of a real electronic state of molecule, the Raman scattering is very strong, which is known as the resonant Raman and is one of effective methods to improve the efficiency of Raman scattering. If the spontaneous nature of the  $j \rightarrow \nu$  transition can be eliminated by using a second field of frequency  $\omega_R$ , the weak Raman scattering can also be enhanced, such as CARS process.

## 2.2 CARS process

The disadvantage of the Raman scattering is the low conversion efficiency due to the small scattering cross-section. Only 1 part out of  $10^6$  of the incident photons will be scattered into the Stokes frequency when propagating through 1cm of a typical Raman active medium. It makes Raman spectroscopy and microscopy more complex and costly that limits its broad applications. As one of nonlinear techniques with coherent nature, intensity of CARS signal is about  $10^5$  stronger than spontaneous Raman. Therefore, the CARS spectroscopy and microscopy have been widely used in physics, chemistry, biology and many other related domains [22-26].

In the CARS process, three laser beams with frequencies of  $\omega_P$ ,  $\omega_{P'}$  and  $\omega_S$  are used as pump, probe and Stokes, the energy level diagram of CARS is shown in figure 2. The primary difference between the CARS and Raman process is that the Stokes frequency stems from an applied laser field in the former. We can simply consider the joint action of the pump and Stokes fields as a source for driving the active Raman mode with the difference frequency  $\omega_P - \omega_S$ . Here, we will first describe CARS process with the classical model, after that a quantum mechanical explanation will be applied for finding the correct expression of the third-order nonlinear susceptibility.

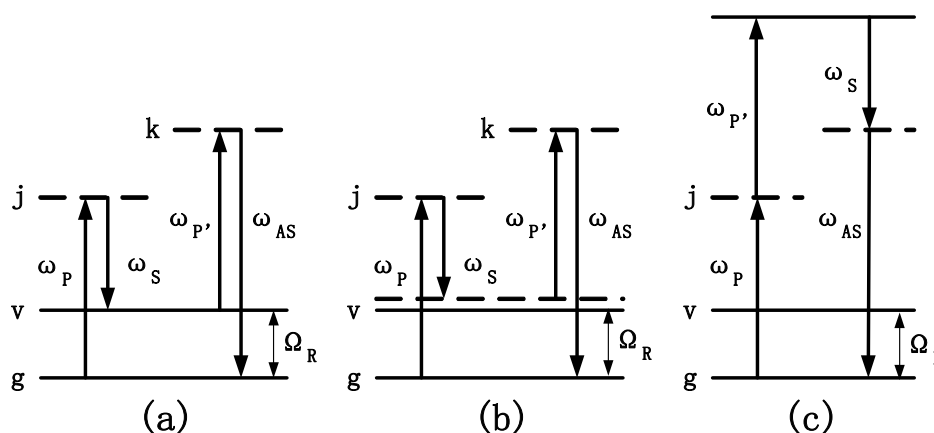


Fig. 2. Energy level diagram of CARS. (a) resonant CARS, (b) nonresonant electronic contribution and (c) electronically enhanced nonresonant contribution. Solid lines indicate real states (g and v); dashed lines denote virtual states (j and k).

### 2.2.1 Classical description of CARS

The classical description of an active vibrational mode driven by the incident optical field is a model of damping harmonic oscillator. The equation of motion for the molecular vibration along  $Q$  is [53]:

$$\frac{d^2Q(t)}{dt^2} + 2\gamma \frac{dQ(t)}{dt} + \omega_v^2 Q(t) = \frac{F(t)}{m}, \quad (2.10)$$

where  $\gamma$  is the damping constant,  $m$  is the reduced nuclear mass, and  $F(t)$  is the external driving force of the oscillation from the incident optical fields. In the CARS process,  $F(t)$  is provided by the incident pump and Stokes fields:

$$F(t) = \left( \frac{\partial \alpha}{\partial Q} \right)_0 E_P E_S^* e^{-i(\omega_P - \omega_S)t}, \quad (2.11)$$

where the time-varying driven force oscillates at the beat frequency of the incident optical fields. A solution to equation (2.10) can be written as:

$$Q = Q(\omega_P - \omega_S) \left\{ e^{-i(\omega_P - \omega_S)t} + e^{i(\omega_P + \omega_S)t} \right\},$$

where  $Q(\omega_P - \omega_S)$  is the amplitude of the molecular vibration. Then, from the equation (2.10), it can be worked out:

$$Q(\omega_P - \omega_S) = \frac{(1/m) [\partial \alpha / \partial Q]_0 E_P E_S^*}{\omega_v^2 - (\omega_P - \omega_S)^2 - 2i(\omega_P - \omega_S)\gamma}. \quad (2.12)$$

From the equation (2.12), we know that the amplitude of molecular vibration is proportional to the product of the amplitudes of the driving fields and the polarizability change. When the frequency difference of the pump and the Stokes fields equals to the resonant frequency  $\omega_v$ , the molecular vibration of active Raman mode will be resonantly enhanced. When a probe field with frequency of  $\omega_{Pr}$  passes through the medium, it will be modulated by the resonant enhanced molecular vibrational mode, resulting in a component at the anti-Stokes frequency,  $\omega_{Pr} + \omega_P - \omega_S$ .

The total nonlinear polarization is the summation of all  $N$  dipoles:

$$P(t) = N\mu(t) = N \left[ \left( \frac{\partial \alpha}{\partial Q} \right)_0 Q \right] E_{Pr}(t). \quad (2.13)$$

In order to simplify the experimental system, the pump field provides the probe field. The frequency of generated anti-Stokes signal is  $\omega_{AS} = 2\omega_P - \omega_S$ . The total nonlinear polarization can be written as:

$$P(t) = P(\omega_{AS}) e^{-i(\omega_{AS})t}. \quad (2.14)$$

With (2.12), (2.13), and (2.14), we can deduce the amplitude of total nonlinear polarization:

$$P(\omega_{AS}) = \frac{(N/m) [\partial \alpha / \partial Q]_0^2}{\omega_v^2 - (\omega_P - \omega_S)^2 - 2i(\omega_P - \omega_S)\gamma} E_P^2 E_S^* = 3\chi_r^{(3)}(\omega_{AS}) E_P^2 E_S^*. \quad (2.15)$$

From above discussion, we know that the amplitude of the total nonlinear polarization is proportional to the product of three incident optical fields. Here, we define the vibrational resonant third-order susceptibility  $\chi_r^{(3)}(\omega_{AS})$ :

$$\chi_r^{(3)}(\omega_{AS}) = \frac{(N/3m) [\partial \alpha / \partial Q]_0^2}{\omega_v^2 - (\omega_P - \omega_S)^2 - 2i(\omega_P - \omega_S)\gamma}. \quad (2.16)$$

It is an inherent property of medium that describes the medium's response to the incident optical fields. When the frequency difference of incident optical fields matches with frequency of a vibrational mode,  $\omega_P - \omega_S = \omega_v$ ,  $\chi_r^{(3)}(\omega_{AS})$  will maximize.

The intensity of CARS signal is proportional to the square modulus of the total polarization:

$$I_{\text{CARS}} \propto |P^{(3)}(\omega_{AS})|^2 = 9 |\chi_r^{(3)}(\omega_{AS})|^2 I_P^2 I_S. \quad (2.17)$$

It scales quadratically with the pump intensity, linearly with the Stokes intensity, and quadratically with the third-order susceptibility of the medium.

Although the classical description of CARS can provide a picture of CARS process and a simplified relationships among the medium, intensities of incident optical fields and CARS signals, it is unable to account for the interaction of the fields with the quantized states of the molecule. More accurate numerical estimates can only be achieved with a quantum mechanical description of the CARS process.

## 2.2.2 Quantum mechanical description of CARS

The quantum mechanism of CARS process can be effectively described by the time-dependent third-order perturbation theory. In the quantum mechanical description, the system is usually expressed in terms of the density operator:

$$\rho(t) \equiv |\psi(t)\rangle\langle\psi(t)| = \sum_{nm} \rho_{nm}(t) |n\rangle\langle m|, \quad (2.18)$$

where the wave functions are expanded in a basis set  $\{|n\rangle\}$  with time-dependent coefficients  $c_n(t)$ , and  $\rho_{nm}(t) \equiv c_n(t)c_m^*(t)$ .

The expectation value for the electric dipole moment is then given by:

$$\langle\mu(t)\rangle = \sum_{n,m} \mu_{mn} \rho_{nm}(t). \quad (2.19)$$

The third-order nonlinear susceptibility for the CARS process is found by calculating the third-order correction to the density operator through time-dependent perturbation theory and with the relation  $\chi_r^{(3)} \equiv N \langle\mu(t)\rangle / 3E_P^2 E_S^*$ :

$$\chi_r^{(3)} = \frac{N}{V} \sum_v \frac{A_v}{\omega_v - (\omega_P - \omega_S) - i\Gamma_v}, \quad (2.20)$$

where  $\Gamma_v$  is the vibrational decay rate that is associated with the line width of the Raman mode R. The amplitude  $A_v$  can be related to the differential scattering cross-section:

$$A_v \propto \frac{(\pi\epsilon_0)^2 c^4 n_P}{\hbar\omega_P\omega_S^3 n_S} (\rho_{gg} - \rho_{vv}) \sigma_{\text{diff}}, R, \quad (2.21)$$

where  $n_P$  and  $n_S$  are the refractive index at the pump and Stokes frequency,  $\rho_{gg}$  and  $\rho_{vv}$  is the element of the density matrix of the ground state and vibrationally excited state,

respectively. The CARS signal intensity is again estimated by substituting equation (2.20) into (2.7).

The quantum mechanical description of CARS process can be qualitatively presented by considering the time-ordered action of each laser field on the density matrix  $\rho_{nm}(t)$ . Each electric field interaction establishes a coupling between two quantum mechanical states of the molecule, changing the state of the system as described by the density matrix. Before interaction with the laser fields, the system resides in the ground state  $\rho_{gg}$ . An interaction with the pump field changes the system to  $\rho_{jg}$ . Then the system is converted into  $\rho_{vg}$  by the following Stokes field. The density matrix now oscillates at frequency  $\omega_{vg} = \omega_{jg} - \omega_{vj}$  that is a coherent vibration. When the third incident optical field interact with medium, the coherent vibration can be converted into a radiating polarization  $\rho_{kg}$ , which propagates at  $\omega_{kg} = \omega_{jg} + \omega_{vg}$ . After emission of the radiation, the system is brought back to the ground state.

As a coherent Raman process, the intensity of CARS signal is more than five orders of magnitude greater than that of spontaneous Raman scattering process. Because the radiating polarization is a coherent summation, the intensity of CARS signal is quadratic in the number of Raman scattering. Because of the coherence, the CARS signal is in certain direction that allows a much more efficient signal collection than Raman scattering. CARS signal is blue-shifted from incident beams, which avoids the influence from any one-photon excited fluorescence.

## 2.3 Resonant and nonresonant signals in CARS

### 2.3.1 Source of nonresonant background signals

From the theory of the CARS process, we can know that CARS signal comes from the third-order nonlinear susceptibility. The total CARS signal is proportional to the square modulus of the nonlinear susceptibility [46]:

$$I(\omega_{AS}) \propto \left| \chi^{(3)}(\omega_{AS}) \right|^2 = \left| \chi_r^{(3)}(\omega_{AS}) \right|^2 + \left| \chi_{nr}^{(3)} \right|^2 + 2\chi_{nr}^{(3)} \operatorname{Re} \left\{ \chi_r^{(3)}(\omega_{AS}) \right\}. \quad (2.22)$$

The total third-order nonlinear susceptibility is composed of a resonant ( $\chi_r^{(3)}$ ) and a nonresonant ( $\chi_{nr}^{(3)}$ ) part:

$$\chi^{(3)} = \chi_r^{(3)} + \chi_{nr}^{(3)}, \quad (2.23)$$

where resonance  $\chi_r^{(3)}$  is a complex quantity,  $\chi_r^{(3)} = \chi_r^{(3)'} + i\chi_r^{(3)''}$  and represents the Raman response of the molecules. When the frequency difference between the pump and Stokes fields equals to the vibrational frequency of an active Raman mode, a strong CARS signal is induced. It provides the inherent vibrational contrast mechanism of CARS microscopy. However, it is not the only components in the total anti-Stokes radiations. In the absence of active Raman modes, the electron cloud still has oscillating components, at the anti-Stokes frequency  $\omega_{AS} = 2\omega_P - \omega_S$ , coupling with the radiation field. It is the purely electronic nonresonant contribution from  $\chi_{nr}^{(3)}$  that is frequency-independent and a real quality. Two energy level diagrams of nonresonant contribution are depicted in figure 2 (b) and (c), when all three incident optical fields overlap in time. As shown in figure 2 (b), a radiating

polarization at  $2\omega_P - \omega_S$  is established via field interactions with virtual levels. When  $2\omega_P$  is close to the frequency of a real electronic state, it is a nonresonant two-photon enhanced electronic contribution, as shown in figure 2 (c). The nonresonant contribution is a source of background that limits the sensitivity of CARS microscopy. For weak vibrational resonances, the nonresonant background may overwhelm the resonant information. In biological samples, the concentration of interested molecules usually is low, while the nonresonant background from the aqueous surrounding is generally ubiquitous. The mixing of the nonresonant field with the resonant field gives rise to the broadened and distorted spectral line shapes. Therefore, the suppression of the nonresonant contribution is essential for practical applications.

### 2.3.2 Suppression of NRB noise

Several effective methods have been developed in order to suppress the NRB noise. Here, we briefly discuss several widely used techniques for suppressing the NRB noise.

#### Epi-detection [54, 55]

In samples, every object will be the source of NRB noise. The aqueous environment produces an extensive NRB noise that may be stronger than the resonant CARS signal from a small object in focus. Because the epi-CARS (E-CARS) has the size-selective mechanism, the NRB noise from the aqueous surrounding can be suppressed while the signal from small objects will be retained. It should be noted that the NRB noise can not be directly reduced in E-CARS. When samples have comparative sizes or in a highly scattering media, such as tissues, this method will not work.

#### Polarization-sensitive detection

The polarization-sensitive detection CARS (P-CARS) is based on the different polarization properties of the resonant CARS and nonresonant signals to effectively suppress the NRB noise [56-58]. According to the Kleinman's symmetry, the depolarization ratio of the nonresonant field is  $\rho_{nr} = \chi_{1221}^{(3)nr} / \chi_{1111}^{(3)nr} = 1/3$  [59]. However, the depolarization ratio of resonant field is  $\rho_r = \chi_{1221}^{(3)r} / \chi_{1111}^{(3)r}$ , which depends on the symmetry of the molecule and may vary from 1/3. The nonlinear polarization, polarized at an angle  $\theta$ , can be written as a function of the angle between the pump and Stokes fields:

$$P^i(\theta) = \frac{3}{4} \chi_{1111}^i \cos \phi \left\{ \bar{e}_x + \rho^i \tan \phi \bar{e}_x \right\} E_P^2 E_S^*, \quad (2.24)$$

where  $i$  is either the resonant or nonresonant component. The nonresonant field is linearly polarized along an angle  $\theta_{nr} = \tan^{-1}(\tan(\phi)/3)$ . When detecting the signal at an angle orthogonal to the linearly polarized nonresonant background, the resonant signal is:

$$P^r(\theta) = \frac{3}{4} \chi_{1111}^r \cos \phi \sin \theta_{nr} (1 - 3\rho^r) E_P^2 E_S^*. \quad (2.25)$$

When  $\phi = 71.6^\circ$  and  $\theta_{nr} = 45^\circ$ , the ratio of resonant and nonresonant signals reaches the maximum. Under this condition, the nonresonant background can be negligible. The P-

CARS has been successfully applied in spectroscopy and microscopy [60]. A schematic of a typical P-CARS system is shown in figure 3.

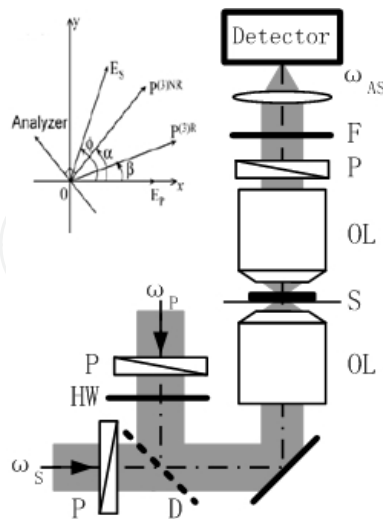


Fig. 3. Schematic of P-CARS. P, polarizer; HW, half-wave plate; D, dichroic beam splitter; OL, objective lens; S, specimen; F, filter.

In a P-CARS system, an analyzer in front of the detector is used to block the nonresonant signal, while the portion of the differently polarized resonant signal passes through the analyzer. Although the P-CARS can effectively suppress the NRB noise, the acquisition time is longer because of the loss of resonant signals

#### Time-resolved CARS detection

In the time-resolved CARS detection (T-CARS), the ultra-short laser pulse is used as excitation laser. The resonant and nonresonant contributions are separated in the time domain due to the different temporal response characteristics [61, 62]. Because of the instantaneous dephasing characteristics of nonresonant signal, it exists only when three laser pulses temporally overlap. In T-CARS, a pair of temporally overlapped laser pulses is used as the pump and Stokes pulse to resonantly enhance the molecular vibration. A laser pulse with time delay is used as the probe pulse. The resonant CARS signal decays in the finite dephasing time of the vibrational mode. The dephasing time is related to the width of spectral line of the corresponding Raman band and is typically several hundred femtoseconds (in solid) to a few picoseconds (in gas or liquid) [63]. Therefore, the NRB noise can be eliminated by introducing a suitable time delay between the pump/Stokes and probe pulses [64]. The detail discussions will be given in the next section.

#### Phase control

In the phase control method, a phase-mismatched coherent addition of nonresonant spectral components is introduced with phase shaping of the femtosecond laser pulses to suppress the nonresonant signal [65-67]. For CARS imaging with picosecond pulses, the phase control can be achieved by heterodyning the signal with a reference beam at the anti-Stokes wavelength [68, 69]. With the heterodyne CARS interferometry, the imaginary part of the third-order nonlinear susceptibility ( $\text{Im}\{\chi_r^{(3)}\}$ ) can be separated to suppress NRB noise [70-72].

## 2.4 Condition of momentum conservation: Phase-matching

Unlike fluorescence or spontaneous Raman microscopy, the CARS process is a parametric process, in which the conditions of energy and momentum must conserve. The generation of CARS signals thus relies on not only the intensity of focused incident optical fields, but the phase conditions of focused fields.

$$l \ll l_c = \pi / |\Delta k|, \quad (2.26)$$

where  $l$  is the effective interaction length,  $l_c$  is the coherent length, the wave-vector mismatch  $\Delta k = k_{AS} - (k_P + k_{P'} - k_S)$ ,  $k_P$ ,  $k_{P'}$ ,  $k_S$  and  $k_{AS}$  is the wave-vector of pump, probe, Stokes and anti-Stokes field respectively. Under the tight focusing condition, in the CARS microscopy with collinear geometry, a small excitation volume and a large cone angle of wave-vectors compensate the wave-vector mismatch induced by the spectral dispersion of the refractive index of the sample, and the phase matching condition can easily be fulfilled [73, 74]. Therefore, the collinear geometry is the best configuration choice of CARS microscopy.

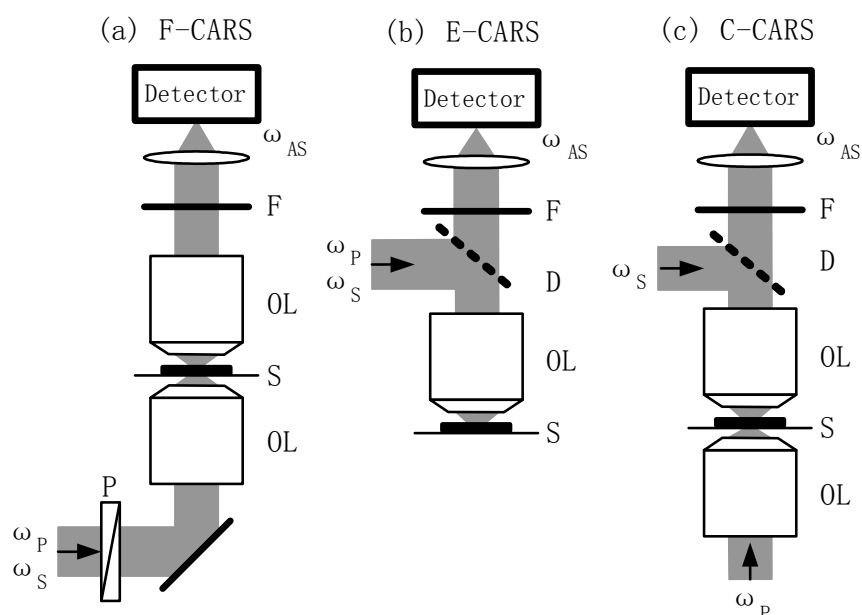


Fig. 4. Schematics of three typical CARS microscopy. (a) forward-detection CARS (F-CARS), (b) epi-CARS (E-CARS), and (c) counterpropagating CARS (C-CARS) microscopy. P, polarizer; D, dichroic beam splitter; OL, objective lens; S, specimen; F, filter.

Three typical geometries of CARS microscopes are shown in figure 4. In figure 4(a) and (b), both the pump and Stokes beams collinearly propagate, and the anti-Stokes signal is detected in the forward direction (a) and backward direction (b). For the forward-detection CARS (F-CARS), the phase matching condition can be easily fulfilled by using an objective with high numerical aperture (NA). For the epi-detection CARS (E-CARS) and counterpropagating CARS (C-CARS) (c) with collinearly propagating geometry, large wave-vector mismatch is introduced and is  $|\Delta k| = 2|k_{AS}| = 4n\pi/\lambda_{AS}$ , and  $|\Delta k| = 2|k_S| = 4n\pi/\lambda_S$ . Here,  $n$  is the refractive index of medium assumed to be independent of frequency. Therefore, the latter two CARS microscopes have higher sensitivity for object of much smaller than the interaction length.

## 2.5 Applications of CARS spectroscopy and microscopy

As one of noninvasive research tools with high sensitivity, specificity and resolution, CARS microscopy has attracted more and more attention and been widely used in physics, chemistry, biology, medicine and life science et al. The capabilities and availability of CARS microscopy has been further improved with the recent technique's advances. Many exciting results have been presented in many literatures.

Because of the label-free characteristic of CARS microscopy, it has been regarded in the biological research, especially in the unstained cells. The first CARS microscopy was used to obtain the structural image of epidermal cells of onion immersed in D<sub>2</sub>O [21]. The water diffusion in live dictyostelium cells was researched with a broad vibrational resonance centered at 3300 cm<sup>-1</sup>, which could not be observed with fluorescence microscopy [75]. These early experimental results have proved that the CARS microscopy is an effective complementary method of fluorescence microscopy. Since many cellular processes take place on a subsecond timescale, high temporal resolution is required. By improving the temporal resolution, it is possible to image the chromosome distribution during mitosis using the symmetric stretching vibration of the DNA phosphate backbone [76]. Because of the good detectability of lipids, the structural and functional images of various living cells were obtained with CH bond of lipid [75, 77-79]. The sensitivity of CARS microscopy is high enough to detect lipid vesicles with sizes smaller than 300 nm in diameter [79]. Compared with fluorescence microscopy, CARS microscopy allows long-term investigations of cell without photobleaching. Therefore it can be used to long-term track biological molecules, such as lipid droplets, in living cells [80]. Nan and associates used the CARS microscopy to study the growth and transport of lipid droplets in live cells [79]. By tuning to the CH<sub>2</sub> lipid vibration, Cheng and his colleagues observed the apoptosis, and identified different stages in the apoptotic process [76]. Potma and his associates visualized the intracellular hydrodynamics with the CARS signal of the O-H stretching vibration of water [81].

On the basis of cell imaging, the CARS microscopy is used in the living animal's tissue imaging, in which the tissue's optical properties, such as absorbability and scattering, are of obvious concern. The method of epi-detection is a good solution in tissue imaging with CARS. CARS microscopy has been successfully used for imaging of nonstained axonal myelin in spinal tissues in vitro [82]. Both the forward and backward CARS signals from the tissue slab were detected. The lipid distributions in skin tissue of live animals have been observed [83]. These all preliminary experimental results show us a vast potential of CARS microscopy in biomedical imaging and early diagnosis of diseases.

## 3. Supercontinuum with photonic crystal fiber

As we have discussed in previous sections, in a CARS spectroscopy or microscopy, it is necessary that two ultra-short laser pulses with high peak power and different frequencies reach focus at the same time. In order to quickly distinguish different molecules in a complex system with the complete CARS spectra, such as various biological molecules in cells, it is required that the output of source must have not only a wide enough spectral range, but the spectral continuity and simultaneity of various spectral components [84]. Spectral broadening and the generation of new frequency components are inherent features of nonlinear optics. When ultra-short laser pulses propagate through a nonlinear medium, a dramatic spectral broadening will happen. This particular physical phenomenon, known as

supercontinuum (SC) generation, was first demonstrated in the early 1970s [85-87]. With the advent of a new kind of optical waveguides in the late 1990s, photonic crystal fiber (PCF) has led to a great revolution in the generation of SC with ultra-broad spectral range and high brightness [39, 88, 89]. In this section, we will introduce the SC generation with PCFs by theoretical analysis and modeling. Based on the requirements of CARS, the method and conditions for realizing an ideal SC source are discussed.

### 3.1 Photonic crystal fiber used for supercontinuum generation

SC generation involves many nonlinear optical effects, such as self- and cross-phase modulation, four-wave mixing (FWM), stimulated Raman scattering (SRS) and solitonic phenomena, which add up to produce a output with an ultra-broadband spectra, sometimes spanning over a couple of octaves. With the developments of theories and techniques of modern nonlinear optics, various optical materials are realized and widely used in various fields. A photonic crystal fiber (PCF) (also called holey fiber (HF) or microstructure fiber (MF)) [90-92], based on the properties of two-dimension photonic crystal, is a kind of special optical fiber, which can confine the incident light passing through the entire length of fiber with its tiny and closely spaced air holes. Different arrangements of the air holes make PCFs with various optical characters, such as the single-mode propagation, high nonlinearity, and controllable dispersion.

According to different guiding mechanism, there are mainly two categories of PCF, photonic bandgap (PBG) PCF [93] and the total internal reflection (TIR) PCF, as shown in figure 5. The PBG PCF is usually used for transmission of high-energy laser pulses and optical signals. The major energy propagates through the hollow core of a PBG PCF with low loss, dispersion and nonlinear effects. The TIR PCF is used for the SC generating with wide spectral range. When high-intensity laser pulses with narrow line-width propagate in a TIR PCFs, the SC, sometimes spanning over a couple of octaves, could be generalized because of its high nonlinearity and group velocity dispersion effects.

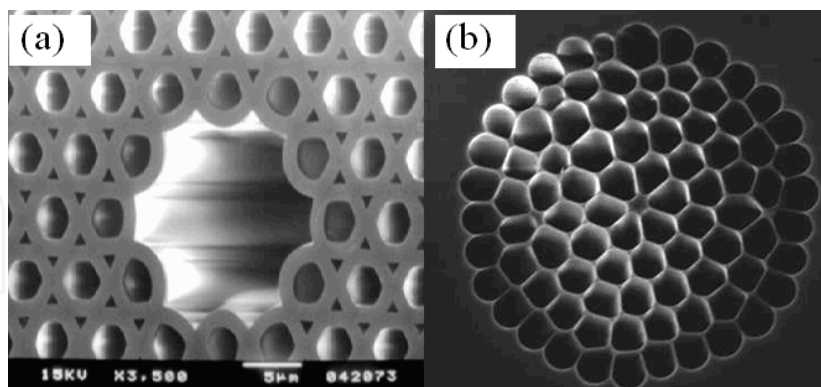


Fig. 5. Structures of a typical PBG PCF (a) and TIR PCF (b) obtained with scanning electron microscope.

### 3.2 Numerical modeling

The process of SC generation is a synthesis result of a variety of the nonlinear optical effects, when ultra-short laser pulses with high intensity propagate in a PCF [94, 95]. Used as the source for CARS, we have mostly concerned about, however, the single-mode propagation

and temporal distributions of various spectral components of SC, called temporal-spectral distribution [96]. For a PCF with a given structure, a number of numerical modeling and computational methods have been constructed and reported to obtain the entire properties of a PCF. Here, we carry out an entire analysis on the SC generation with a common method that is mainly divided into three steps.

Firstly, as one of most effective methods, the finite element method (FEM) can be used to obtain the coefficients of the chromatic dispersion (the effective propagation constant  $\beta_{\text{eff}}$ ) based on the structural parameters of PCFs (the diameter of air-hole, and the pitch between two holes). The dispersion coefficients  $\beta_k$  ( $k \geq 2$ ) can be derived by the Taylor series expansion at the central frequency  $\omega_0$ , and the nonlinear coefficient  $\gamma$  can be approximately calculated by  $\gamma = n_2 \omega_0 / c A_{\text{eff}}$ , with  $n_2$  the nonlinear-index coefficient for silica,  $c$  the speed of light in vacuum, and  $A_{\text{eff}}$  the effective core area.

Secondly, a propagation equation is used to calculate the SC generation during the propagation of ultra-short laser pulses, although the generalized nonlinear Schrödinger Equation (GNLSE) is not the only way to realize it. The process of the pulses propagation was simulated with the split-step Fourier method (SSFM) to solve GNLSE [94].

$$\frac{\partial A}{\partial z} + \frac{\alpha}{2} A - \sum_{k \geq 2} \frac{i^{k+1}}{k!} \beta_k \frac{\partial^k A}{\partial T^k} = i\gamma \left( 1 + \frac{i}{\omega_0} \frac{\partial}{\partial T} \right) \left( A(z, t) \int_{-\infty}^{+\infty} R(T') \times |A(z, T - T')|^2 dT' + i\Gamma_R(z, T) \right). \quad (3.1)$$

In equation (3.1), the linear propagation effects on the left-hand side and nonlinear effects on the right-hand side are given, where  $\alpha$  and  $A$  are the loss coefficient and the spectral envelope with the new time frame  $T = t - \beta_1 z$  at the group velocity  $\beta_1^{-1}$ .  $R(T)$  presents the Raman response function. The noise  $\Gamma_R$ , which affects the spontaneous Raman noise, is neglected,  $\Gamma_R = 0$ . It has more detailed explanation in the paper [94].

For a CARS spectroscopy or microscopy, the temporal-spectral distribution of SC is also an important factor. Therefore, thirdly, we have to figure it out in order to fully understand the temporal distribution of various spectral components in SC, although the spectral envelope of SC can be obtained in the second step. To obtain the temporal-spectral distribution of SC, cross-correlation frequency resolved optical gating method (XFROG) was applied for characteristic of SC and could be proved by an experimental instrument of XFROG [97]. The two-dimensional XFROG spectrogram can be plotted by using two electromagnetic fields and the following equation:

$$I_{\text{XFROG}}(\omega, \tau) = \left| \int_{-\infty}^{+\infty} E(t) E_{\text{gate}}(t - \tau) \exp(-i\omega t) dt \right|^2, \quad (3.2)$$

where  $E(t)$  is the calculated envelope of the SC with the variable  $t$ , and  $E_{\text{gate}}(t - \tau)$  is the gating pulses with the delay time  $\tau$  between the seed laser pulses and the SC. It can be concluded that XFROG measurement is a good way to characterize the temporal and spectral evolution of the SC generation and interpret the particular time and frequency domain information of the optical effects. With the above introduced method, we carried out simulation analysis in

order to find out a way to achieve an ideal SC source for CARS spectroscopy and microscopy. Some representative results will be shown in the next section.

### 3.3 Supercontinuum generation with photonic crystal fiber

Some of our computational results are shown here in order to account for the whole processing course clearly. We have simulated the SC generation by using a PCF with two zero dispersion wavelengths (ZWD) [98]. The calculated group velocity dispersion (GVD) curve is shown in figure 6. By solving GNLS with SSFM, the temporal and spectral distributions of the SC generation along the whole length of PCF are shown in figure 7. With the XFROG trace, the results of temporal-spectral distributions of PCFs with different lengths are described in figure 8.

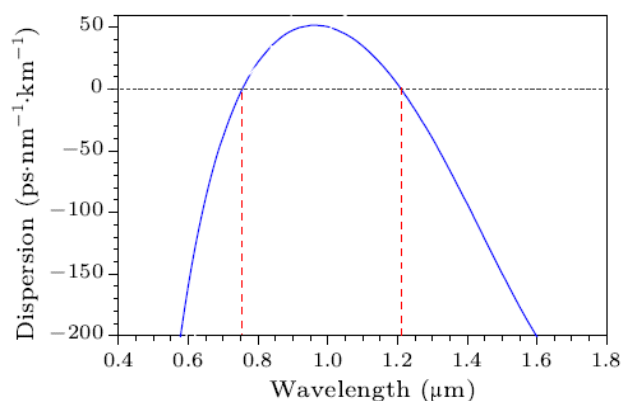


Fig. 6. Group velocity dispersion curve of the PCF with two ZWDs [98].

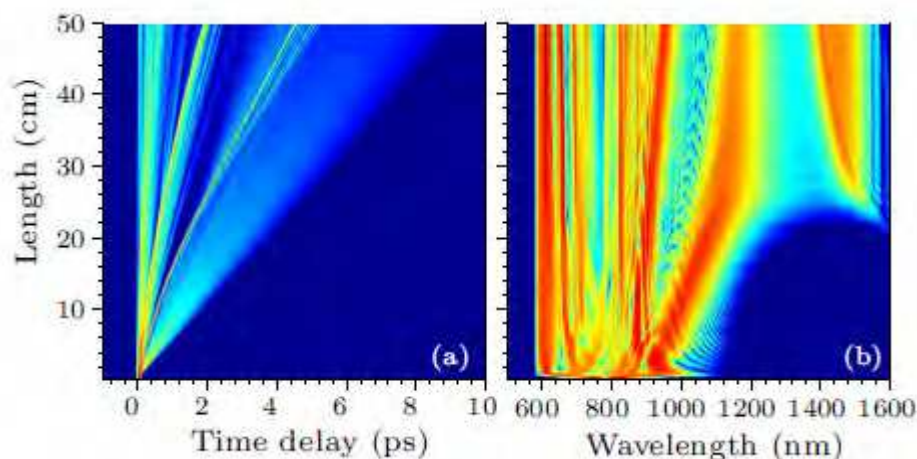


Fig. 7. Time (a) and spectrum (b) evolution of SC along the entire length of the PCF with the input pulse width 30 fs and peak power 10 kW [98].

In figure 8(c), the spectral range of generated SC is 500nm by using a PCF with two ZDW under proper pumping conditions. In SC, the spectral continuity, simultaneity and intensity of red-shifted SC components are all good enough for a source of CARS. But for this purpose, an ultra-short pulse laser system with pulse width of 30fs is needed, which is not easily sustainable during practically experimental operations. Therefore, we have tried to seek a

simpler way to generate favorable SC for CARS applications. The simulation results are shown in figure 9, where we can see that the SC generated by a PCF with two ZDW is quite good for CARS applications when the laser pulse width is 300fs, as shown in figure 9 (c).

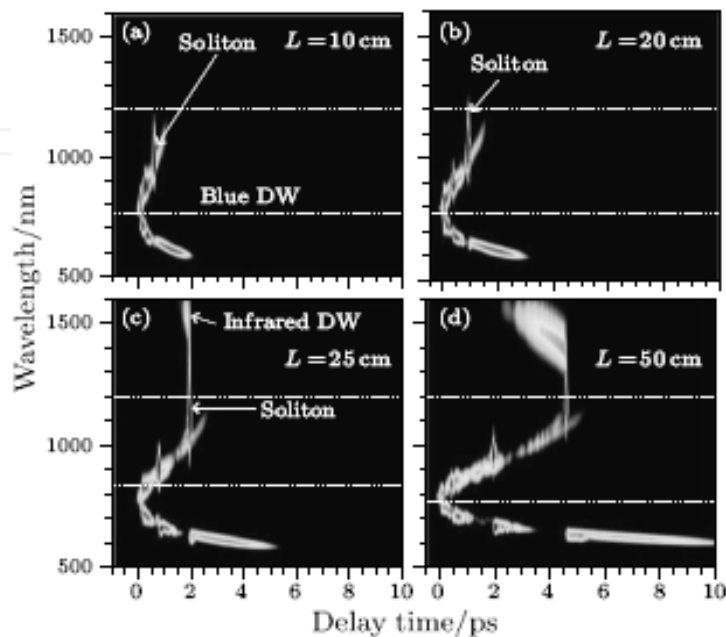


Fig. 8. Temporal-spectral distribution of SC when PCFs with lengths of 10 cm (a), 20 cm (b), 25 cm (c), and 50 cm (d) pumped by laser pulse with pulse-width 30 fs, wavelength 780 nm, and peak power 10 kW [98].

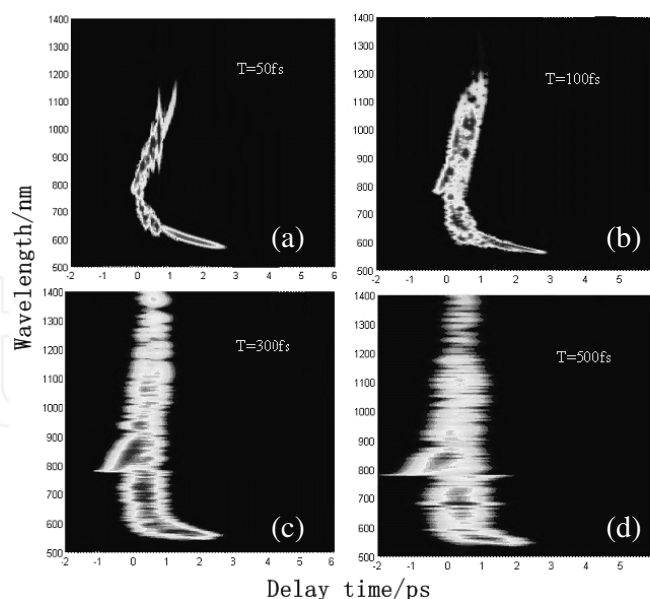


Fig. 9. Temporal-spectral distribution of the SC when using the femtosecond laser pulse with a central wavelength of 780 nm, peak power of 10 kW and pulse-width of 50 fs (a), 100 fs (b), 300 fs (c) and 500 fs (b) as seed pulse to pump a PCF with length of 10cm.

By numerical simulations, we clearly understood the effects of the parameters of PCF and pumping laser pulse on the generation of SC. All simulation results provide us an intuitive

description of SC generation, and theoretical guides for experimental instruments. Dispersion and nonlinearity of a PCF can be modified and optimized by adjusting the air-hole structure of a PCF. Under specifically experimental conditions, a perfect SC source for CARS spectroscopy and microscopy can be achieved with an optimized PCF.

#### 4. Broadband CARS spectroscopy and microscopy

In a traditional CARS microscopy, two or three ultra-short laser pulses with narrow line-width and different frequencies are used as excitation beams. It permits high-sensitivity imaging based on a particular molecular bond, called single-frequency CARS. But for a mixture with various or unknown components, it is not adequate to distinguish the interested molecules from a complex based on the signal of a single active Raman bond. The broadband even complete molecular vibrational spectra will be beneficial for obtaining the accurate information of various chemical compositions. Although it can be achieved by sequentially tuning the frequency of Stokes beam, it is time-consuming and unpractical for some applications. This problem can be circumvented by using the multiplex CARS (M-CARS) or broadband CARS spectroscopy with simultaneously detected wider band.

##### 4.1 Introduction to broadband CARS

The M-CARS spectroscopy was first demonstrated by Akhmanov et al., a part of CARS spectra of a sample can be simultaneously obtained [34]. In M-CARS, a broadband laser beam is used as the Stokes beam for providing a required spectral range. A narrow line-width laser beam is used as the pump and probe beam that determines the spectral resolution of the system. The multiplex molecular vibrational modes of a sample can be resonantly enhanced, the corresponding CARS signals can be detected simultaneously, the energy diagram of M-CARS shown in figure 10.

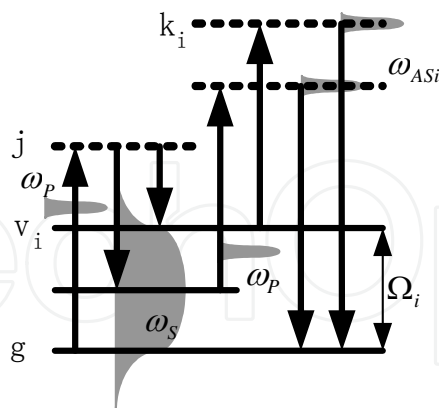


Fig. 10. Energy level diagram of M-CARS.

In the previous works, a narrowband and a broadband dye laser was used for the pump/probe and the Stokes beams respectively [36-38]. The recent progress in wavelength-tunable ultra-short pulse laser has been giving a powerful momentum to the development of M-CARS. The M-CARS micro-spectroscopy has been developed for fast spectral characterization of microscopic samples [35, 99, 100]. But because of the used laser limitation to the line-width, M-CARS is still unable to simultaneously obtain wider molecular

vibrational spectra as required. With the progress of SC generation technique [85-87], especially with the advent of PCF [39], much wider spectra of M-CARS can be simultaneously obtained by broadening the spectral range of Stokes pulses with nonlinear optical fiber, such as the tapped optical fiber [101] or PCF [43, 44, 102]. By using a specially designed and achieved SC source, the simultaneously detectable spectral range of M-CARS spectroscopy and microscopy is greatly widened, which can be called the broadband CARS. Wider simultaneously detectable spectral range makes it possible to quickly distinguishing various components and real-time monitoring slight variations in a mixture [103-105]. At the same time, the system of the broadband CARS with SC is simplified and cost is reduced.

#### 4.2 Suppression of NRB noise in broadband CARS with SC

In the M-CARS, NRB noise can not be avoided and many methods for suppressing it in a single-frequency CARS can also be used, but they can not be easily applied in the broadband CARS with SC, because of the complex polarization and phase of various spectral components in SC, as shown in section 3. The NRB noise can be eliminated with numerical fitting method by regarding it as a reference signal, but the Raman spectra of the samples are needed in advance [106].

As presented in above section, the time-resolved detection method can effectively eliminate the NRB noise by introducing a temporal delay between pump/Stokes pulses and probe pulse in order to temporally separate the resonant and nonresonant signals. In a T-CARS, three laser pulses, with frequencies at  $\omega_P$ ,  $\omega_{P'}$ , and  $\omega_S$ , are used as the pump, probe and Stokes pulses respectively. The generation process of CARS signals can be described in three phases [107]. In the first phase, the inherent molecular vibration of active Raman mode is driven by simultaneous pump and Stokes pulses and is resonantly enhanced when  $\Omega_R = \omega_P - \omega_S$ . The amplitude of resonantly enhanced molecular vibration is [108]:

$$\frac{\partial Q_v}{\partial t} + \frac{Q_v}{T_2} = \frac{i}{4m\Omega_r} \left( \frac{\partial \alpha}{\partial Q} \right) E_p E_S^* (1 - 2n_a), \quad (4.1)$$

where  $Q_v$  is the amplitude of molecular vibration driven by the incident optical fields,  $T_2$  is the dephasing time of the resonant enhanced molecular vibrational state. When the simultaneous ultrashort laser pulses are used as the pump and Stokes pulses, the intensity changes of  $Q_v$  with time is shown in figure 11.  $Q_v$  increases during the period of incident laser pulses and reaches its maximum when the pump and Stokes pulses just disappear.

In the second phase, with the disappearance of incident laser pulses, the resonantly enhanced molecular vibration will rapidly return to its original state that can be regarded as a free relaxation process. Equation (4.1) can be rewritten as [107]:

$$\frac{\partial Q_v}{\partial t} = -\frac{Q_v}{T_2}. \quad (4.2)$$

The solution of equation (4.2) is [107]:

$$|Q_v|^2 = A \exp(-2t/T_2), \quad (4.3)$$

where  $A$  is an integration constant. We can see that  $Q_v$  decays exponentially with time immediately after disappearance of the pump and Stokes pulses. Assuming the dephasing time is 10ps, the relaxation process of  $Q_v$  is shown in figure 12.

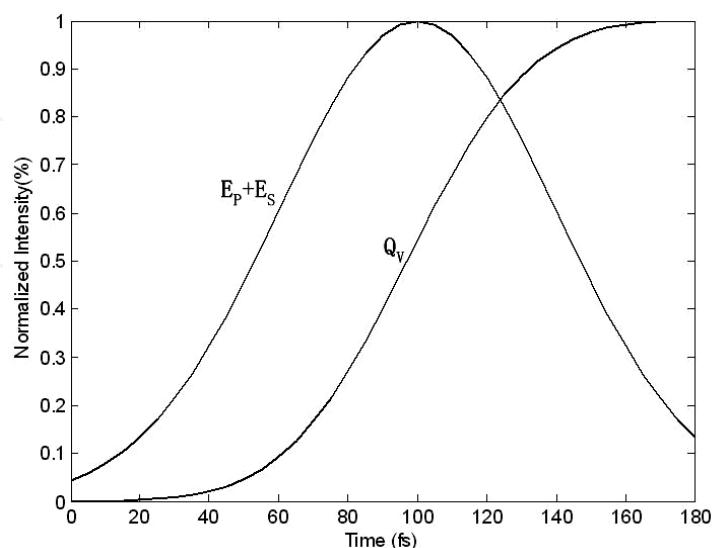


Fig. 11. Intensity of  $Q_v$  amplitude versus time, when the vibration of active Raman mode is resonantly enhanced by incident pump and Stokes pulses [107].

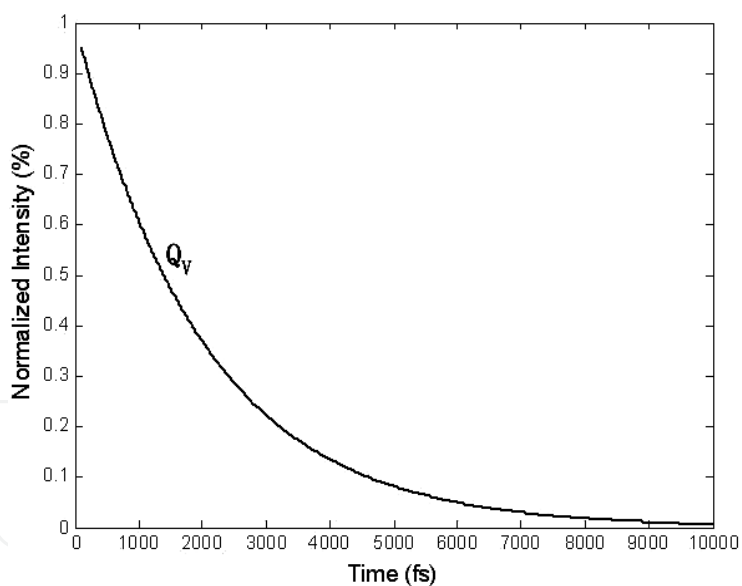


Fig. 12. The free relaxation process of a molecular vibration mode immediately after disappearance of the pump and Stokes laser pulses [107].

In the third phase, when the probe pulse reaches the focus with the delay time  $t_D$ , it will be modulated by the resonantly enhanced molecular vibration. The signal field at anti-Stokes frequency is generated and can be expressed as [107]:

$$\frac{\partial E_{AS}}{\partial z} + \frac{n_{AS}}{c} \frac{\partial E_{AS}}{\partial t} + \frac{\alpha_{AS}}{2} E_{AS} = \frac{i\omega_{AS}}{2n_{AS}c\epsilon_0} \left[ \frac{1}{2} N \left( \frac{\partial \alpha}{\partial Q} \right) E_p Q_v e^{-i\Delta k z} \right]. \quad (4.4)$$

From the equation (4.4), we can find that the CARS signal field does not include the nonresonant component  $\chi_{nr}^{(3)}$  that disappears with the end of the pump and Stokes pulses simultaneously. When the phase-matching condition is satisfied,  $\Delta k=0$ , the intensity changes of the CARS signal with time is shown in figure 13.

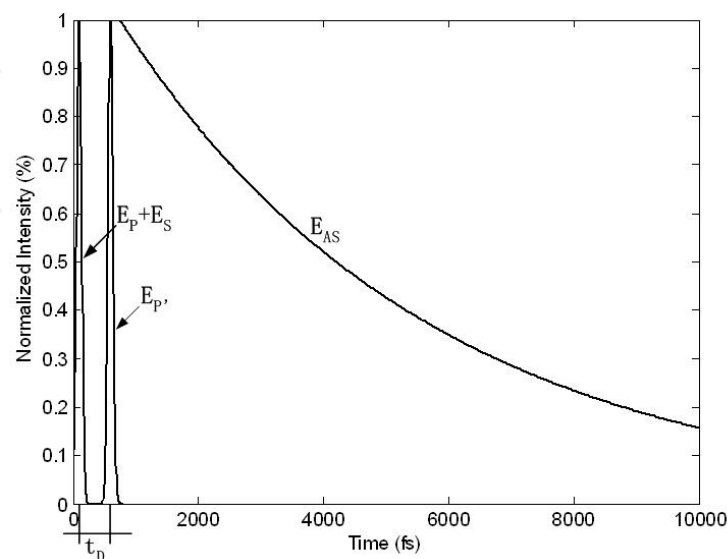


Fig. 13. Intensity of CARS signal changes with time [107].

In the T-CARS method, the resonant and nonresonant components have different temporal response characteristics. In order to effectively separate the resonant and nonresonant contributions and avoid the intensity loss of the CARS signal, the pulse-width of simultaneous pump and Stokes pulse should be as short as possible and the rising edge of the probe pulse should be as steep as possible.

Recently the broadband T-CARS spectroscopy and microscopy with SC has been rapidly developed [43, 44], whose energy level diagram is shown in figure 14. In the broadband T-CARS, a well-designed SC is used as the pump and Stokes pulses and a temporally delayed laser pulse is used as the probe pulse. The simultaneously detectable spectral range and the spectral resolution are determined by the temporally overlapped spectral range of the SC and by the line-width of the probe pulse respectively. With the improvement of temporal-spectral distribution of the SC, the simultaneously detectable spectral range of system can be further extended, which is called the ultra-broadband T-CARS and will be discussed in detail in the next section.

### 4.3 Ultra-broadband T-CARS spectroscopy with SC generated by PCF<sup>[84, 96]</sup>

With a broadband T-CARS spectroscopy, we can obtain more specificities of the sample, not only the vibrational spectra reflecting the molecular structure and compositions, but also the dephasing time of various molecular vibrational modes reflecting the molecular responses to the external micro-environment, which are especially favorable for the study of the complicated interaction processes between molecules and their micro-environment such as solute-solvent interactions [108, 109], molecular dynamics<sup>[110-114]</sup>, supramolecular structures<sup>[115]</sup> and excess energy dissipations in the fields of biology, chemistry and material science [64, 116-118].

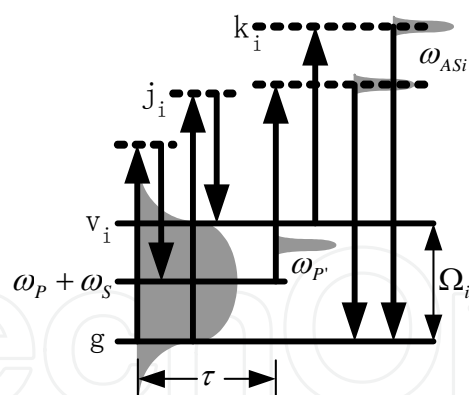


Fig. 14. Energy level diagram of the broadband T-CARS.

The principle of broadband T-CARS spectroscopy has been presented in section 4.2. As discussed in section 3 and 4, the simultaneously detectable spectral range of a broadband T-CARS spectroscopy is limited by the simultaneously generated spectral range and its continuity in the SC. An ultra-broadband T-CARS spectroscopy based on optimized SC has been developed to simultaneously obtain CARS signals corresponding to various molecular vibrational modes and Raman free induction decays (RFID) of these molecular vibrational modes in a single measurement [43, 84]. The schematic of the broadband T-CARS spectroscopy is shown in figure 15. A femtosecond laser pulse of a mode-locked Ti:sapphire laser oscillator (Mira900, Coherent) is split into two parts by a beam splitter. One beam of the laser pulse, used as the seed pulse, is introduced into a PCF with geometric length of 180 mm and ZDW of 850 nm respectively. After passing through a long-pass filter, the residual spectral components of SC are used as the pump and the Stokes. Another beam is used as the probe pulse after passing through a narrow-band-pass filter. Two beams of the laser pulses are collinearly introduced into a microscope and tightly focused into a sample with an achromatic microscopy objective. The generated CARS signals in the forward direction, passing through a short-pass filter, are collected with the same microscope objective and detected by a fibre spectrometer. The delay time between SC pulse and probe pulse can be accurately adjusted by a kit of time delay line.

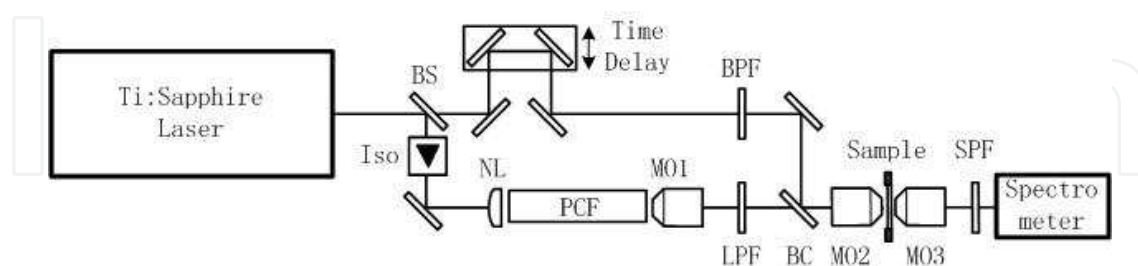


Fig. 15. The schematic of the ultra-broadband T-CARS system. BS, beam splitter; Iso, optical isolator; NL, non-spherical lens; PCF, photonic crystal fibre; BC, beam combiner; MO1-3, microscopy objective; BPF, narrow-band-pass filter; LPF, long-pass filter; SPF, short-pass filter [84].

With the ultra-broadband T-CARS spectroscopy, the time-resolved measurement is achieved by adjusting the delay time between the SC pulse and the probe pulse step by step [84]. The obtained time-resolved CARS spectral signals and CARS signals at specific delay

time of pure benzonitrile and mixture solution are shown in figure 16. The molecular vibrational spectra for pure liquid benzonitrile in the range of 380-4000  $\text{cm}^{-1}$  can be simultaneously obtained without any tuning of the system and its characteristics. The NRB noise can be effectively suppressed through tuning the delay time. For the pure benzonitrile, the obvious peaks at wavenumbers of 1016  $\text{cm}^{-1}$ , 1190  $\text{cm}^{-1}$ , 1608  $\text{cm}^{-1}$ , 2248  $\text{cm}^{-1}$  and 3090  $\text{cm}^{-1}$  correspond to C-C-C trigonal breathing, C-H in plane bending, C-C in plane stretching, C $\equiv$ N stretching, and C-H stretching vibrational modes respectively [119]. In the mixture, the peaks at wavenumbers of 1016  $\text{cm}^{-1}$ , 2248  $\text{cm}^{-1}$  and 3090  $\text{cm}^{-1}$  of benzonitrile can be apparently seen [120]. Other peaks correspond to the typical molecular vibrational modes of methanol and ethanol. We can easily and accurately distinguish the various components in the mixture. The spectral resolution, depending on the line-width of the probe pulse and spectral resolution of the spectrometer, is 14  $\text{cm}^{-1}$  in this case.

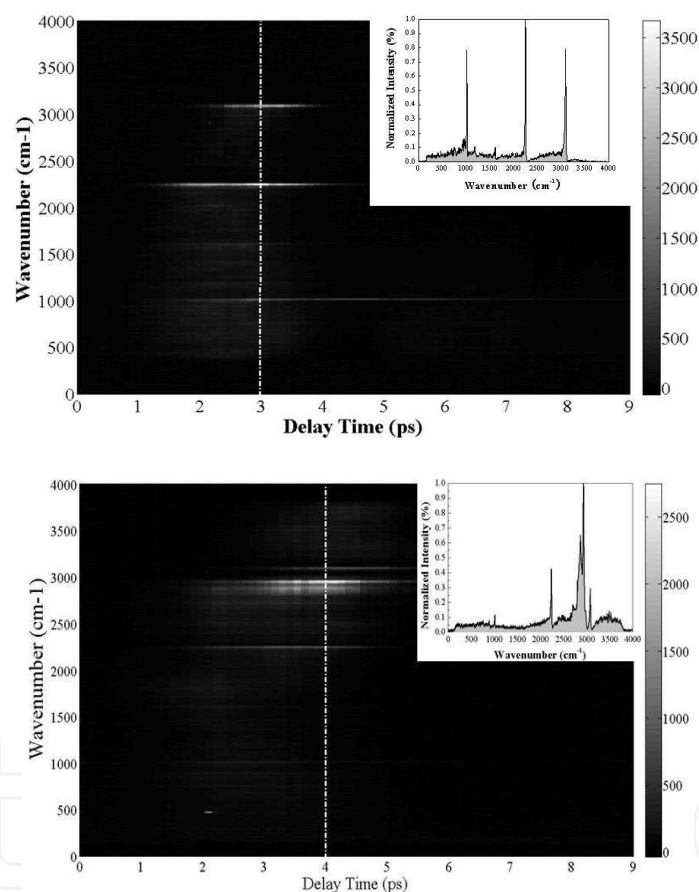


Fig. 16. Intensities of time-resolved CARS signals of pure benzonitrile and at the delay time of 3 ps (a). Intensities of time-resolved CARS signals of benzonitrile-methanol-ethanol mixture solution and at the delay time of 4 ps (b) detected with the ultra-broadband T-CARS spectroscopy [84].

By extracting the time evolutions of CARS signals corresponding to the molecular vibrational modes for a pure liquid benzonitrile and mixture, the RFID processes of various molecular vibrational modes can be measured at the same time. The dephasing times of various molecular vibrational modes can be obtained by fitting the data to a single exponential function as:

$$I(\tau) = A_0 \exp(-2\tau/T), \quad (4.5)$$

where  $T$  is the vibrational dephasing time responding to each molecular vibrational mode;  $A_0$  is a constant;  $\tau$  is the delay time. The normalized intensities of five typical peaks corresponding to typical molecular vibrational modes for pure benzonitrile, at the wavenumbers of  $1016 \text{ cm}^{-1}$ ,  $1190 \text{ cm}^{-1}$ ,  $1608 \text{ cm}^{-1}$ ,  $2248 \text{ cm}^{-1}$  and  $3090 \text{ cm}^{-1}$ , are plotted one by one as a function of  $\tau$  and fitted to equation (4.5) in figure 17 (a)-(e) respectively [84].

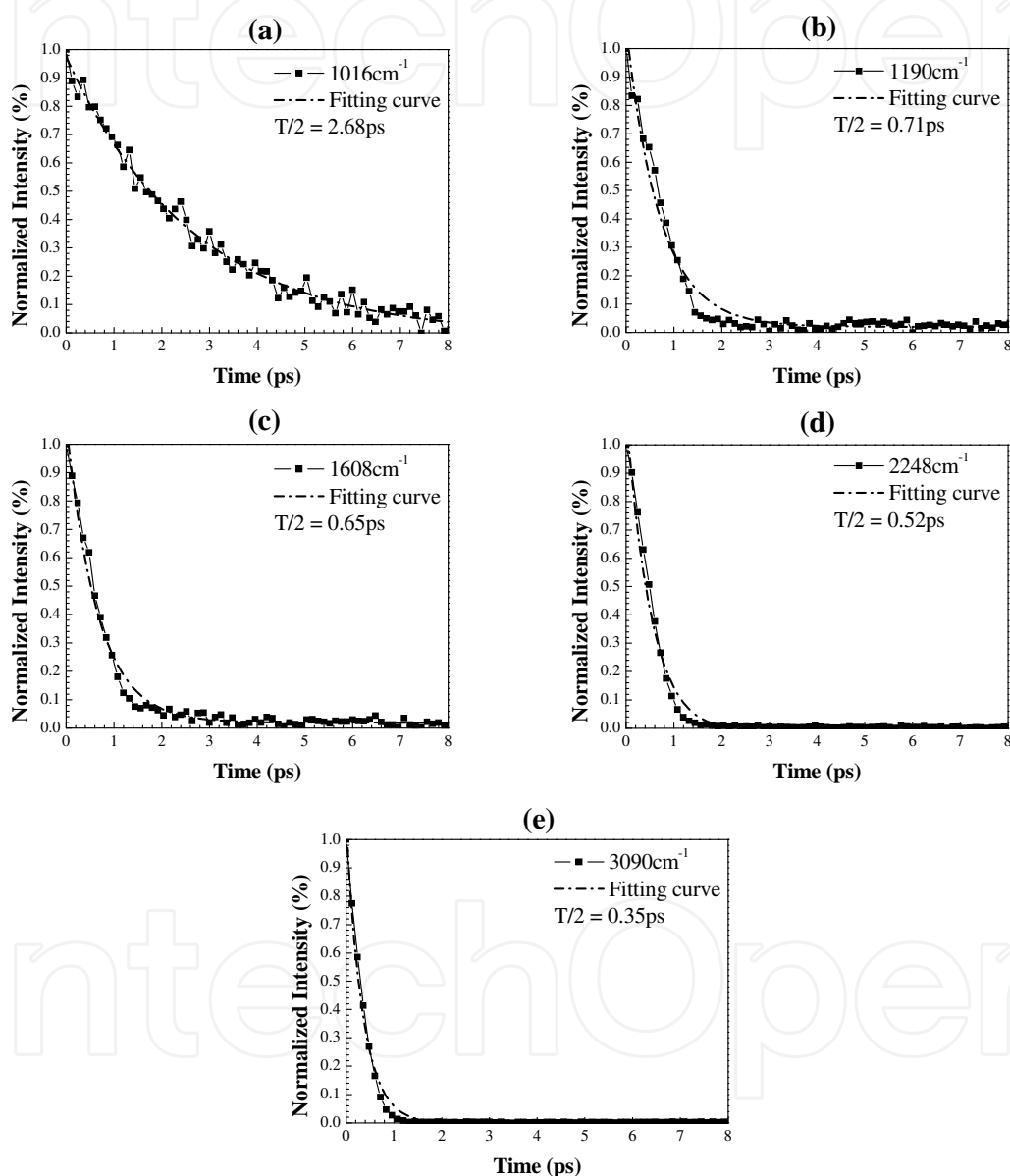


Fig. 17. Vibrational dephasing processes and their relevant dephasing times of various molecular vibrational modes for pure liquid benzonitrile shown in (a)-(e) respectively, with the solid line corresponding to the change of CARS signal with delay time and the dash dot line representing the fitting curve to a single exponential function [84].

In a benzonitrile-methanol-ethanol mixture solution, the benzonitrile molecule is regarded as the target molecule. The normalized intensities of three typical peaks corresponding to

typical molecular vibrational modes for benzonitrile, at the wavenumbers of  $1016\text{ cm}^{-1}$ ,  $2248\text{ cm}^{-1}$  and  $3090\text{ cm}^{-1}$ , are plotted one by one as a function of  $\tau$  and fitted to equation (4.5) in figure 18 (a)-(c), respectively.

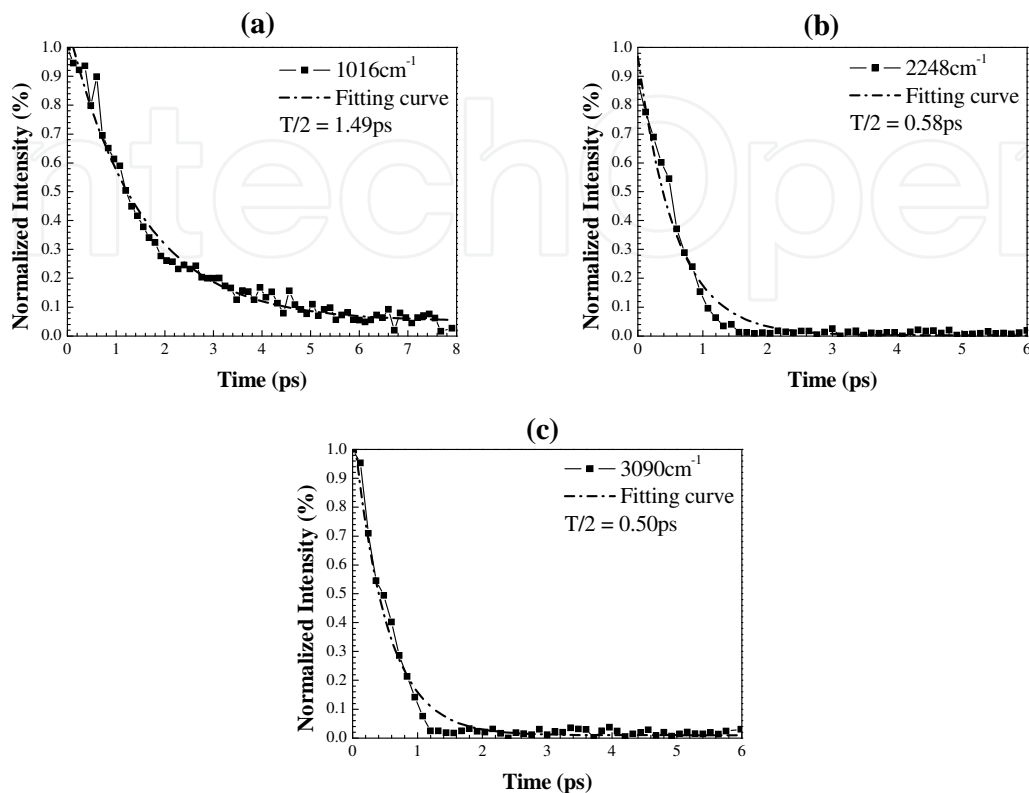


Fig. 18. Vibrational dephasing processes and their corresponding dephasing times of various molecular vibrational modes for benzonitrile in benzonitrile-methanol-ethanol mixture solution shown in (a)-(c) respectively, with the solid line corresponding to the variation of CARS signal with delay time and the dash dot line representing the single exponential fitting curve [84].

From experimental results, the intensities of the CARS signals corresponding to different molecular vibrational modes attenuate exponentially against the delay time in a large dynamic range. By fitting the intensity data of the CARS signal to a single exponential function for the molecular vibrational modes at different wave-numbers, half of vibrational dephasing time  $T/2$  can be worked out as shown in figure 17, which are consistent with the previously published data [43, 121-123]. But in a benzonitrile-methanol-ethanol mixture solution, the experimental results show that the influence of solvent on the property of solute is reflected not by the Raman peak position but by the variations of the vibrational dephasing times for different molecular vibrational modes.

#### 4.4 Simultaneously obtaining the complete molecular vibrational spectra

As discussed above, the simultaneously detectable spectral range of the ultra-broadband T-CARS with SC depends on the quality of the SC. It is of importance to simultaneously obtain the complete molecular vibrational spectra and the dephasing times of various molecular vibrational modes of the sample. The former is very useful for effectively and accurately

distinguishing various kinds of components and understanding the mechanisms of chemical reactions in a dynamic process. The latter is very helpful for explanation of both solvent dynamics and solute-solvent interactions in the fields of biology, chemistry and material science. The question is whether we can reach above goal in the near future by optimizing the temporal-spectral distribution of the SC? Our answer is positive. As what we have known the existing molecules have the Raman wave-numbers in the range of about tens to 5000  $\text{cm}^{-1}$ , which means that the simultaneously generated Stokes wavelength bandwidth should be not less than 350nm. As we have given in section 3 that the bandwidth of the simultaneously generated SC can be greater than 400nm, therefore it is very promising to achieve label-free microscopic imaging technique with high contrast and chemical specificity based on the simultaneously obtained complete molecular vibrational spectra.

## 5. Sub-diffraction-limited CARS microscopy

### 5.1 Methods of improving spatial resolution of CARS microscopy

As well known, there is a theoretical limitation of the spatial resolution for any far-field optical microscopes because of the existence of light diffraction. Ernst Abbe defined the diffraction limit as [124]:

$$d = \frac{0.61\lambda}{n \sin \phi} \cong \frac{\lambda}{2NA}, \quad (5.1)$$

where  $d$  is the resolvable minimum size,  $\lambda$  is the wavelength of incident light,  $n$  is the refraction index of the medium being imaged in,  $\phi$  is the aperture angle of the lens, and  $NA$  is the numerical aperture of the optical lens. It is obvious that for an optical microscope,  $d$  is the theoretical limit of spatial resolution. The samples' spatial features, smaller than approximately half the wavelength of the used light, would never be able to be resolved.

In recent years, in order to meet the requirements on the study of life science and material science, ones have found several ways to overcome the optical diffraction limit and obtained sub-diffraction limited spatial resolution theoretically. In fluorescence microscopy, the success of the resolution enhancement techniques relies on the ability to control the emissive properties of fluorophores with a proper optical beam. The most important developments for breaking through the diffraction barrier are sub-diffraction-limited resolution fluorescent imaging techniques, such as photo activated localization microscopy (PALM) [125], stochastic optical reconstruction microscopy (STORM) [126], and stimulated emission depletion (STED) microscopy [127, 128], which have opened up notable prospect for sub-cellular structure and bio-molecular movement and interaction imaging.

As one of label-free nonlinear imaging techniques, the spatial resolution of CARS microscopy is higher (about 300nm lateral resolution) than the one of traditional linear optical microscopy, but it is still a diffraction-limited imaging technique. Today, how to achieve a sub-diffraction-limited CARS microscopy has become one of attractive topics all over the world. Compared with developments of the fluorescence nanoscopy, the method for breaking through the diffraction limitation in CARS microscopy is still under theoretical research.

In 2009, Beeker et al. firstly presented a way to obtain a sub-diffraction-limited CARS microscopy in theory [129]. With the density matrix theoretical calculations, they found that

the molecular vibrational coherence in CARS can be strongly suppressed by using an annular mid-infrared laser to control the pre-population of the corresponding vibrational state. The energy level diagram is shown in figure 19. Thereby the emission of generated CARS signals in the annular area of point spread function could be significantly suppressed and the spatial resolution can be improved considerably.

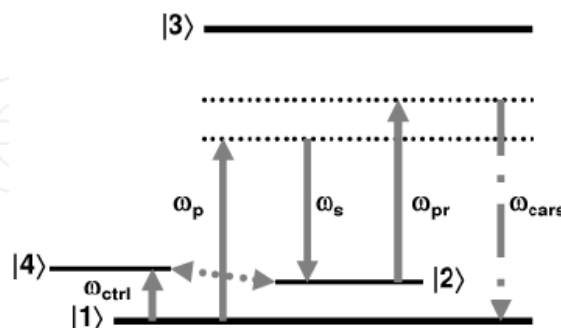


Fig. 19. Energy level diagram for CARS extended with an additional level  $|4\rangle$ . Energy level  $|1\rangle - |4\rangle$  are ground state, vibrational state, excited vibrational state and control state, respectively.  $\omega_p$ ,  $\omega_{pr}$ ,  $\omega_s$ , and  $\omega_{ctrl}$  are the frequencies of pump, probe, Stokes and control laser [129].

Alexei Nikolaenko et al provided their CARS interferometric theory in the same year [130]. In this theoretical research, a stabilized, phase-adjustable interferometer was used to achieve nearly complete interference between the local oscillator and the pump- and Stokes-induced CARS radiation. The schematic of the CARS interferometry setup is shown in figure 20. Their theoretical analysis showed that the energy loss in the anti-Stokes channel is accompanied by an energy gain in the pump and Stokes channels. This implied that the CARS interferometry provided a controllable switching mechanism of anti-Stokes radiation from the focal volume, which might be a possible technique for improving the spatial resolution of the CARS microscopy.

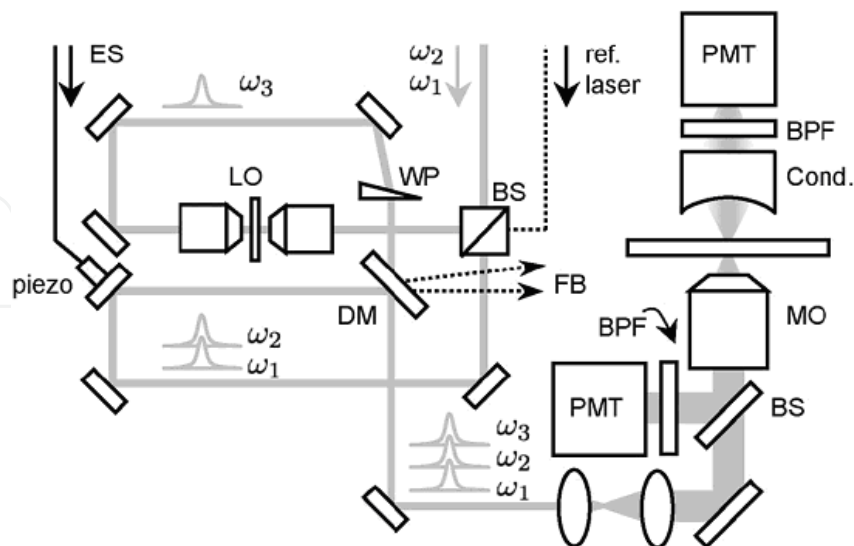


Fig. 20. Schematic of the CARS interferometry. ES, error signal; LO, unit for generating local oscillator; WP, wedged plate; BS, 50-50 beam splitter; DM, dichroic mirror; FB, optical feedback signal; MO, microscope objective; BPF, bandpass filter; Cond., condenser; PMT, photomultiplier [130].

Kim M. Hajek et al presented a theoretical analysis and simulation of a wide-field CARS microscopy with sub-diffraction-limited resolution in 2010 [131]. The configuration and a simulation result are shown in figure 21. In this method, two coherent pump beams were used and interfered in the sample plane, forming a standing wave with variable phase. The numerical simulation showed that a super-resolved image with three times better lateral resolution could be obtained by image processing method of standing-wave frequency theory.

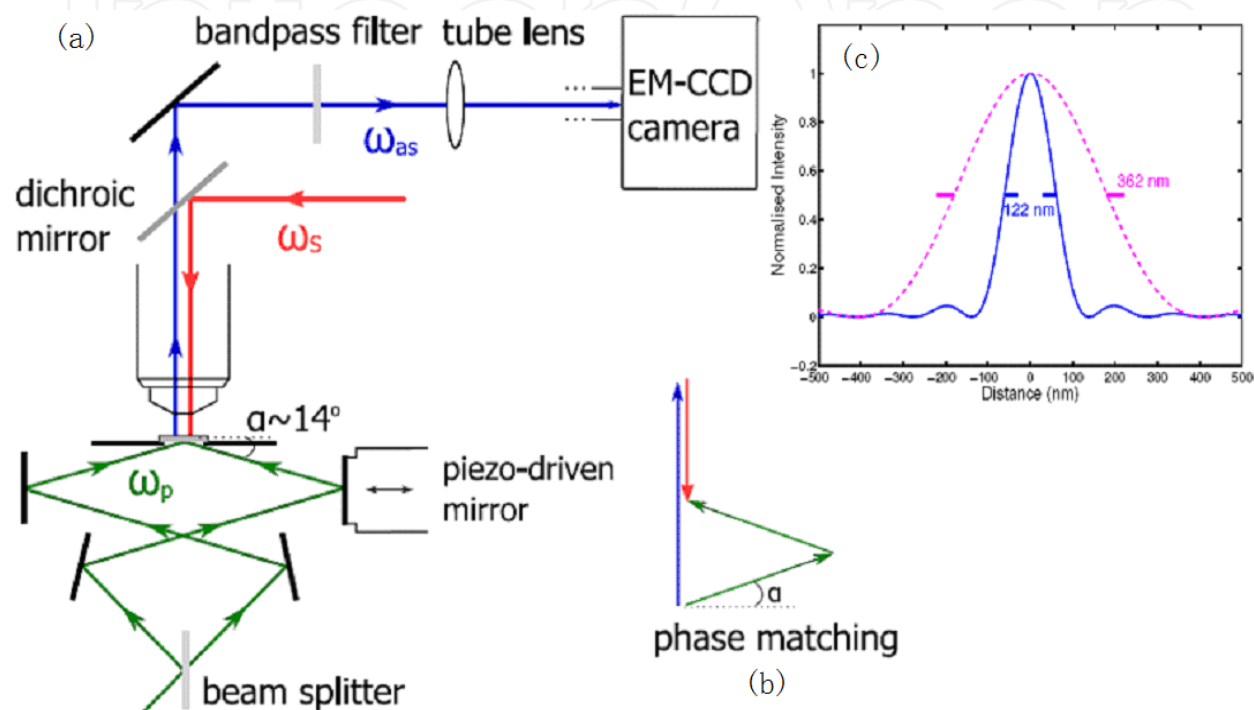


Fig. 21. (a) Schematic of stand-wave wide-filed CARS microscopy, (b) phase-matching condition, (c) simulation result of the point spread function (PSF) of the proposed method [131].

All above discussed sub-diffraction-limited CARS microscopy open up the possibility of achieving sub-diffraction-limited CARS microscopy. Unfortunately, these approaches can only be used in the single frequency CARS microscopy based on the signal of a single molecular vibrational mode.

## 5.2 Phonon depletion CARS microscopy<sup>[132]</sup>

As discussed above, successful methods of breaking through the theoretical diffraction limitation of CARS microscopy depend on the controllable emissive properties of the useful signals in the focus. But the above suggested methods for breaking through the diffraction limited resolution can only be used for dealing with the single bond signal. By researching the CARS process with quantum optics theory, we presented our method for breaking through the diffraction limitation, unlike the above methods, which is effective for ultra-broadband T-CARS microscopy.

In our theoretical model, all incident laser fields, generated signal field and the material system are all described with quantum mechanics theory. In the CARS process, the first light-matter

interaction process involves resonant enhancements of all active molecular vibrational modes, in which the frequency differences of pump and Stokes fields equal the inherent vibrational frequencies of the molecular bonds respectively. The resonantly enhanced molecular vibrations exist in quantized forms which are called the phonons. Their numbers are equal to the numbers of generated Stokes photons respectively. When a probe field propagates through the matter, the photons of the probe interact with the generated phonons. The photons with anti-Stokes frequencies are generated, and phonons are annihilated at the same time.

Based on the whole quantized picture of the CARS process, we presented a phonon depletion CARS (PD-CARS) technique by introducing an additional probe beam with the frequency different from the one of the probe beam in the center of the focus. When the pump and Stokes simultaneously reaches the focus, the phonons are generated. The additional probe beam, which is shaped into a doughnut profile at the focus with a phase mask, reaches the focus a little bit earlier than the probe beam in the center of the focus. Therefore the wavelengths of the generated anti-Stokes signals at the peripheral region differ from the ones at the center of the focus and can be easily separated with a proper interference filter. By this way, the spatial resolution of the ultra-broadband T-CARS microscopy can be improved greatly. The simulation result of PSF is defined as [132]:

$$\Delta r = \sqrt{2} \frac{\lambda}{\pi n \sin \alpha \sqrt{3 + \frac{I_{P1}^{\max}}{I_{dep}}}} \approx \frac{0.9}{\sqrt{3 + \frac{I_{P1}^{\max}}{I_{dep}}}} \cdot \frac{\lambda}{2n \sin \alpha}, \quad (5.2)$$

where  $I_{dep}$  and  $I_{P1}^{\max}$  are intensities of phonon field at the center of the focus and additional probe field for phonon depletion in the annular region respectively. From equation (5.2), we can know that the spatial resolution of CARS microscopy will be improved by increasing the intensity of additional probe beam. The simulation result of PSF is shown in figure 22. When  $I_{P1}^{\max}$  is fiftyfold of  $I_{det}$ , the spatial resolution of the ultra-broadband T-CARS microscopy reaches 41nm.

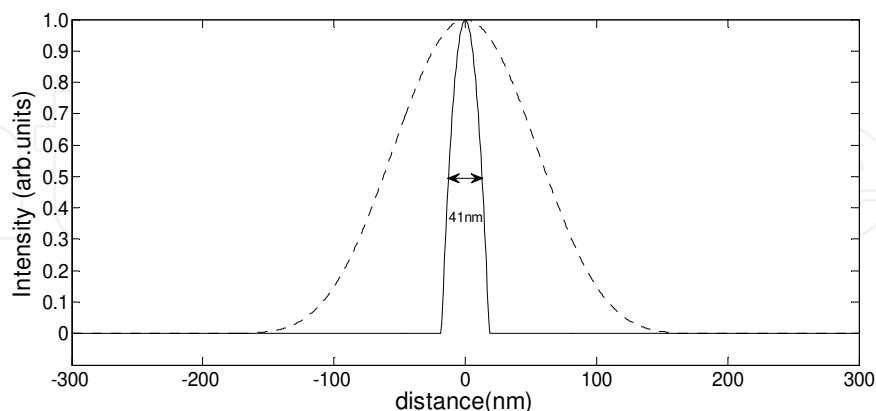


Fig. 22. Simulation result of the PSF in the PD-CARS microscopy [132].

## 6. Conclusions and prospects

In this chapter, we mainly introduce a kind of noninvasive label-free imaging technique – the ultra-broadband T-CARS spectroscopy and microscopy with SC generated by PCF. We

describe the mechanisms of Raman scattering and T-CARS process with the classical and quantum mechanical theory. The CARS signals with much stronger strength and well-oriented direction originate from the coherent resonant enhancement between incident lights and molecular vibrations. In order to quickly and accurately distinguish different kinds of molecules in a complex, such as in a live cell, a method for simultaneously detecting the ultra-broadband CARS signals without the NRB noise has to be developed. On the basis of theoretical analysis and simulation of the SC generation with a PCF, a satisfied SC source can be achieved for obtaining the ultra-broadband even complete CARS spectra of the specimen by optimizing the parameters and the other experimental conditions of the PCF and ultra-short laser. At the same time, the NRB noise can be effectively suppressed in a broad spectral range with the time-resolved method. The method study for obtaining sub-diffraction limited spatial resolution is still on the stage of theoretical research. Some original techniques are presented in this chapter. The PD-CARS technique provides a possible route to the realization of ultra-broadband T-CARS microscopy with sub-diffraction limited spatial resolution, which will probably become an attractive imaging method in biology, medicine and life science in the near future.

## 7. References

- [1] R P Haugland, Handbook of Fluorescent Probes and Research Chemicals, Eugene, OR: Molecular Probes, 1996.
- [2] R Y Tsien and A Miyawaki, Biochemical imaging: Seeing the Machinery of Live Cells, Science, 1998, 280(5371): 1954-1955.
- [3] E Kohen and J G Hirschberg, Cell structure and function by microspectrofluorometry, San Diego, CA: Academic, 1989.
- [4] J B Pawley, Handbook of Biological Confocal Microscopy, New York: Plenum, 1995.
- [5] T Wilson and C Sheppard, Theory and Practice of Scanning Optical Microscopy, Orlando, FL: Academic, 1984.
- [6] W Denk, J H Strickler and W W Webb, Two-photon laser scanning fluorescence microscopy, Science, 1990, 248(4951): 73-76.
- [7] Xu C, W Zipfel, J B Shear, et al, Multiphoton fluorescence excitation: new spectral windows for biological nonlinear microscopy, Proc. Natl. Acad. Sci. U.S.A., 1996, 93: 10763-10768.
- [8] J Hoyland, Fluorescent and Luminescent Probes for Biological Activity, ed. W T Mason. San Diego, CA: Academic, 1999.
- [9] G T Boyd, Y R Shen and T Hansch, Continuous-wave second-harmonic generation as a surface microprobe, Opt. Lett., 1986, 11(2): 97-99.
- [10] U Gauderon, P B Lukins, and C J R Sheppard, Three-dimensional second-harmonic generation imaging with femtosecond laser pulses, Opt. Lett., 1998, 23(15): 1209-1211.
- [11] J C Paul, C M Andrew, T Mark, et al, Three-dimensional high-resolution second-harmonic generation imaging of endogenous structural proteins in biological tissue, Biophys. J., 2002, 82(1): 493-508.
- [12] I Freund and M Deutsch, Second-harmonic microscopy of biological tissue, Opt. Lett., 1986, 11(2): 94-96.
- [13] R M Williams, W R Zipfel and W W Webb. Interpreting second-harmonic generation images of collagen I fibers, Biophys. J., 2005, 88:1377-1386.

- [14] Y Barad, H Eisenberg, M Horowitz and Y Silberberg, Nonlinear scanning laser microscopy by third harmonic generation, *Appl. Phys. Lett.*, 1997, 70(8): 922-924.
- [15] D D Vbarre, W Supatto, A M Pena, et al, Imaging lipid bodies in cells and tissues using third-harmonic generation microscopy, *Nat. Methods*, 2006, 3: 47-53.
- [16] H J Humecki, *Practical Spectroscopy* vol 19, ed. E G Brame Jr, New York: Dekker, 1995.
- [17] G Turrell and J Corset, *Raman Microscopy Development and Applications*, Academic, San Diego, Calif., 1996.
- [18] G J Puppels, F F M De Mul, C Otto, et al, Studying single living cells and chromosomes by confocal Raman microspectroscopy. *Nature*, 1990, 347: 301-303.
- [19] N M Sijtsma, S D Wouters, C J De Grauw, et al, Confocal direct imaging Raman microscope: design and applications in biology, *Appl. Spectrosc.*, 1998, 52(3): 348-355.
- [20] C W Freudiger, W Min, B G Saar, et al, Label-Free Biomedical Imaging with High Sensitivity by Stimulated Raman Scattering Microscopy, *Science*, 2008, 322(5909): 1857-1861.
- [21] M D Duncan, J Reintjes and T J Manuccia, Scanning coherent anti-Stokes Raman microscope, *Opt. Lett.*, 1982, 7(8): 350-352.
- [22] A Zumbusch, G R Holtom and X S Xie, Three-Dimensional Vibrational Imaging by Coherent Anti-Stokes Raman Scattering, *Phys. Rev. Lett.*, 1999, 82(20): 4142-4145.
- [23] M Hashimoto, T Araki and S Kawata, Molecular vibration imaging in the fingerprint region by use of coherent anti-Stokes Raman scattering microscopy with a collinear configuration, *Opt. Lett.*, 2000, 25(24): 1768-1770.
- [24] E O Potma, W P de Boeij and D A Wiersma, Nonlinear coherent four-wave mixing in optical microscopy, *J. Opt. Soc. Am. B*, 2000, 17(10): 1678-1684.
- [25] E O Potma, W P de Boeij, P J M van Haastert, et al, Real-time visualization of intracellular hydrodynamics in single living cells, *Proc. Natl. Acad. Sci. U.S.A.*, 2001 98(4): 1577-1582.
- [26] J X Cheng, A Volkmer and X S Xie, Theoretical and experimental characterization of coherent anti-Stokes Raman scattering microscopy, *J. Opt. Soc. Am. B*, 2002, 19(6): 1363-1375.
- [27] P D Maker and R W Terhune, Study of optical effects due to an induced polarization third order in the electric field strength, *Phys. Rev.*, 1965, 137(3A): 801-818.
- [28] R F Begley, A B Harvey and R L Byer, Coherent anti-Stokes Raman spectroscopy, *Appl. Phys. Lett.*, 1974, 25(7): 387-390.
- [29] Shen Y R, *The Principles of Nonlinear Optics*, New York: Wiley, 1984.
- [30] M D Levenson and S S Kano, *Introduction to Nonlinear Laser Spectroscopy*, San Diego, CA: Academic, 1988.
- [31] S Maeda, T Kamisuki and Y Adachi, *Advances in Non-Linear Spectroscopy*, ed. R J H Clark and R E Hester, New York: Wiley, 1988.
- [32] J Nibler, *Advances in Non-Linear Spectroscopy*, ed. R J H Clark and R E Hester, New York: Wiley, 1988.
- [33] J X Cheng, E O Potma and X S Xie, Coherent anti-Stokes Raman scattering correlation spectroscopy: Probing dynamical processes with chemical selectivity, *J. Phys. Chem. A*, 2002, 106(37): 8561-8568.

- [34] S A Akhmanov, N I Koroteev and A I Kholodnykh, Excitation of the coherent optical phonons of  $E_g$ -type in calcite by means of the active spectroscopy method, *J. Raman Spectrosc.*, 1974, 2(3): 239-248.
- [35] C Otto, A Voroshilov, S G Kruglik, et al, Vibrational bands of luminescent zinc(II)-octaethylporphyrin using a polarization-sensitive 'microscopic' multiplex CARS technique, *J. Raman Spectrosc.*, 2001, 32(6): 495-501.
- [36] L Ujj, B L Volodin, A Popp, et al, Picosecond resonance coherent anti-Stokes Raman spectroscopy of bacteriorhodopsin: spectra and quantitative third-order susceptibility analysis of the light-adapted BR-570, *Chem. Phys.*, 1994, 182(2-3): 291-311.
- [37] B N Toleutaev, T Tahara and H Hamaguchi, Broadband ( $1000\text{ cm}^{-1}$ ) multiplex CARS spectroscopy: Application to polarization sensitive and time-resolved measurements, *Appl. Phys. B*, 1994, 59(4): 369-375.
- [38] A Voroshilov, C Otto and J Greve, Secondary structure of bovine albumin as studied by polarization-sensitive multiplex CARS spectroscopy, *Appl. Spectrosc.*, 1996, 50(1): 78-85.
- [39] P St J Russell, *Photonic Crystal Fibers*, Science, 2003, 299(5605): 358-362.
- [40] H Kano, H Hamaguchi, Near-infrared coherent anti-Stokes Raman scattering microscopy using supercontinuum generated from a photonic crystal fiber, *Appl. Phys. B*, 2005, 80(2): 243-246.
- [41] T W Kee, H X Zhao and M T Cicerone, One-laser interferometric broadband coherent anti-Stokes Raman scattering, *Opt. Expr.*, 2006, 14(8): 3631-3640.
- [42] Lee Y J, Liu Y X and M T Cicerone, Characterization of three-color CARS in a two-pulse broadband CARS spectrum, *Opt. Lett.*, 2007, 32(22): 3370-3372.
- [43] Lee Y J and M T Cicerone, Vibrational dephasing time imaging by time-resolved broadband coherent anti-Stokes Raman scattering microscopy, *App. Phys. Lett.*, 2008, 92(4): 041108.
- [44] Yu L Y, Yin J, Niu H B, et al, Study on the method and experiment of time-resolved coherent anti-Stokes Raman scattering using supercontinuum excitation, *Acta Phys. Sin.*, 2010, 59(8): 5406-5411 (in Chinese).
- [45] D C Harris and M D Bertolucci, *Symmetry and Spectroscopy: An Introduction to Vibrational and Electronic Spectroscopy*, Dover Publications, 1989.
- [46] A Smekal, *Zur Quantentheorie der Dispersion*, *Naturwissenschaften*, 1923, 11: 873-875.
- [47] C V Raman and K S Krishnan, A New Type of Secondary Radiation, *Nature*, 1928, 121(3048): 501-502.
- [48] C V Raman, A New Radiation, *Indian Journal of Physics*, 1928, 2: 387-398.
- [49] G Placzek, Rayleigh-Streuung und Raman-Effekt. In: *Handbuch der Radiologie*. ed. E Marx, Akademische Verlagsgesellschaft, Leipzig, 1934.
- [50] H A Kramers and W Heisenberg, *Über die streuung von strahlen durch atome*, *Z. Phys.*, 1925, 31: 681.
- [51] R Loudon, *The Quantum Theory of Light*, Oxford University Press, Oxford, 1978.
- [52] M O Scully and M S Zubairy, *Quantum Optics*, Cambridge University Press, Cambridge, 1996.
- [53] E Garmire, F Pandarese and C T Townes, Coherently Driven Molecular Vibrations and Light Modulation, *Phys. Rev. Lett.*, 1963, 11(4): 160-163.

- [54] J X Cheng, A Volkmer, L D Book, and X S Xie, An epi-detected coherent anti-Stokes Raman scattering (E-CARS) microscope with high spectral resolution and high sensitivity, *J. Phys. Chem. B*, 2001, 105(7): 1277-1280.
- [55] A Volkmer, J X Cheng and X S Xie. Vibrational imaging with high sensitivity via epi-detected coherent anti-Stokes Raman scattering microscopy, *Phys. Rev. Lett.*, 2001, 87(2): 023901-023904.
- [56] S A Ahkmanov, A F Bunkin, S G Ivanov and N I Koroteev. Coherent ellipsometry of Raman scattered light, *JETP Lett.*, 1977, 25(9): 416-420.
- [57] J L Oudar, R W Smith and Y R Shen, Polarization-sensitive coherent anti-Stokes Raman spectroscopy, *Appl. Phys. Lett.*, 1979, 34(11): 758-760.
- [58] R Brakel and F W Schneider, Polarization CARS spectroscopy In *Advances in Nonlinear Spectroscopy*, ed Clark RJH and Hester RE, JohnWiley & Sons Ltd., New York, 1988.
- [59] D A Kleinman, Nonlinear dielectric polarization in optical media, *Phys. Rev.*, 1962, 126(6): 1977-1979.
- [60] J X Cheng, L D Book and X S Xie, Polarization coherent anti-Stokes Raman scattering microscopy, *Opt. Lett.*, 2001, 26(17): 1341-1343.
- [61] A Laubereau and W Kaiser, Vibrational dynamics of liquids and solids investigated by picosecond light pulses, *Rev. Mod. Phys.*, 1978, 50(3): 607-665.
- [62] F M Kamga and M G Sceats, Pulse-sequenced coherent anti-Stokes Raman scattering spectroscopy: a method for the suppression of the nonresonant background, *Opt. Lett.*, 1980, 5(3): 126-127.
- [63] M Fickenscher, M G Purucker and A Laubereau, Resonant vibrational dephasing investigated with high-precision femtosecond CARS, *Chem. Phys. Lett.*, 1992, 191(1-2): 182-188.
- [64] A Volkmer, L D Book and X S Xie, Time-resolved coherent anti-Stokes Raman scattering microscopy: imaging based on Raman free induction decay, *Appl. Phys. Lett.*, 2002, 80(9): 1505-1507.
- [65] D Oron, N Dudovich and Y Silberberg, Single-pulse phase-contrast nonlinear Raman spectroscopy, *Phys. Rev. Lett.*, 2002, 89(27): 273001-273004.
- [66] N Dudovich, D Oron and Y Silberberg, Single-pulse coherently controlled nonlinear Raman spectroscopy and microscopy, *Nature*, 2002, 418(8): 512-514.
- [67] D Oron, N Dudovich and Y Silberberg, Femtosecond Phase-and-polarization control for background-free coherent anti-Stokes Raman spectroscopy, *Phys. Rev. Lett.*, 2003, 90(21): 213901-213904.
- [68] G Marowsky and G Luepke, CARS-background suppression by phase-controlled nonlinear interferometry, *Appl. Phys. B*, 1990, 51(1): 49-50.
- [69] Y Yacoby and R Fitzgibbon, Coherent cancellation of background in four-wave mixing spectroscopy, *J. Appl. Phys.*, 1980, 51(6): 3072-3077.
- [70] C L Evans, E O Potma and X S Xie, Coherent anti-Stokes Raman scattering spectral interferometry: determination of the real and imaginary components of nonlinear susceptibility for vibrational microscopy, *Opt. Lett.*, 2004, 29(24): 2923-2925.
- [71] D L Marks and S A Boppart, Nonlinear interferometric vibrational imaging, *Phys. Rev. Lett.*, 2004, 92(12):123905.
- [72] C Vinegoni, J S Bredfeldt, D L Marks and S A Boppart, Nonlinear optical contrast enhancement for optical coherence tomography, *Opt. Express*, 2004, 12(2):331-341.

- [73] E O Potma, W P de Boeij and D A J Wiersma, Nonlinear coherent four-wave mixing in optical microscopy, *Opt. Soc. Am. B*, 2000, 17(10): 1678-1684.
- [74] G C Bjorklund, Effects of focusing on third-order nonlinear processes in isotropic media, *IEEE J. Quantum Electron.*, 1975, 11(6): 287-296.
- [75] E O Potma, X S Xie, L Muntean, et al, Chemical Imaging of Photoresists with Coherent Anti-Stokes Raman Scattering (CARS) Microscopy, *J. Phys. Chem. B*, 2004, 108(4): 1296-1301.
- [76] J X Cheng, Y K Jia, G Zheng, and X S Xie, Laser-scanning coherent anti-Stokes Raman scattering microscopy and application to cell biology, *Biophys. J.*, 2002, 83(1): 502-509.
- [77] J X Cheng, L D Book and X S Xie, Polarization coherent anti-Stokes Raman scattering microscopy, *Opt. Lett.*, 2001, 26(17): 1341-1343.
- [78] A Zumbusch, G R Holtom and X S Xie, Three-dimensional vibrational imaging by coherent anti-Stokes Raman scattering, *Phys. Rev. Lett.*, 1999, 82(20): 4142-4145.
- [79] X L Nan, J X Cheng and X S Xie, Vibrational imaging of lipid droplets in live fibroblast cells with coherent anti-Stokes Raman scattering microscopy, *J. Lipid. Res.*, 2003, 44(11): 2202-2208.
- [80] X L Nan, E O Potma and X S Xie, Nonperturbative Chemical Imaging of Organelle Transport in Living Cells with Coherent Anti-Stokes Raman Scattering Microscopy, *Biophys. J.*, 2006, 91(2): 728-735.
- [81] E O Potma, W P d Boeij, P J M van Haastert and D A Wiersma, Real-time visualization of intracellular hydrodynamics in single living cells, *Proc. Natl. Acad. Sci. U.S.A.*, 2001, 98(4): 1577-1582.
- [82] H Wang, Y Fu, P Zickmund, R Shi and J X Cheng, Coherent anti-Stokes Raman scattering imaging of axonal myelin in live spinal tissues, *Biophys. J.*, 2005, 89(1): 581-591.
- [83] C L Evans, E O Potma, M Puoris'haag, et al, Chemical imaging of tissue in vivo with video-rate coherent anti-Stokes Raman scattering (CARS) microscopy, *Proc. Natl. Acad. Sci. USA*. 2005. 102(46): 16807-16812.
- [84] Yin Jun, Yu Ling-yao, Niu Han-Ben, et al, Simultaneous measurements of global vibrational spectra and dephasing times of molecular vibrational modes by broadband time-resolved coherent anti-Stokes Raman scattering spectrography, *Chin. Phys. B*, 2011, 20(1): 014206.
- [85] R R Alfano and S L Shapiro, Emission in the region 4000 to 7000 Å via four-photon coupling in glass, *Phys. Rev. Lett.*, 1970, 24(11): 584-587.
- [86] R R Alfano and S L Shapiro, Observation of self-phase modulation and small-scale filaments in crystals and glasses, *Phys. Rev. Lett.*, 1970, 24(11): 592-594.
- [87] R R Alfano, *The Supercontinuum Laser Source*, ed. R. Alfano, Springer, Berlin, 1989.
- [88] J K Ranka, R S Windeler and A J Stentz, Visible continuum generation in air-silica microstructure optical fibers with anomalous dispersion at 800 nm, *Opt. Lett.*, 2000, 25(1): 25-27.
- [89] J C Knight, Photonic crystal fibres, *Nature*, 2003, 424: 847-851.
- [90] J C Knight and P St J Russell, New ways to guide light, *Science*, 2002, 296(5566): 276-276.
- [91] T A Birks, J C Knight and P St J Russell, Endlessly single-mode photonic crystal fiber, *Opt. Lett.*, 1997, 22(13): 961-963.

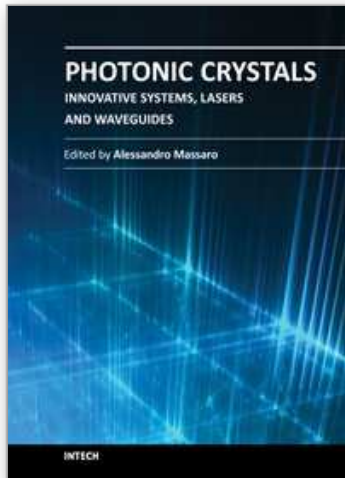
- [92] J C Knight, J Broeng, T A Birks, et al. Photonic band gap guidance in optical fibers, *Science*, 1998, 282(5393): 1476-1478.
- [93] R F Cregan, B J Mangan, J C Knight, et al. Single-mode photonic band gap guidance of light in air, *Science*, 1999, 285(5433): 1537-1539.
- [94] J M Dudley, G Genty and S Coen, Supercontinuum generation in photonic crystal fiber, *Rev. Mod. Phys.*, 2006, 78 (4): 1135-1184.
- [95] G P Agrawal, *Nonlinear Fiber Optics* (4<sup>th</sup> ed.), Elsevier, 2007.
- [96] Yin Jun, Ph D. Thesis, 2010.
- [97] Q Cao, X Gu, E Zeek, et al, Measurement of the intensity and phase of supercontinuum from an 8-mm-long microstructure fiber, *Appl. Phys. B*, 2003, 77(2-3):239-244.
- [98] Liu Xing, Yin Jun, Niu Han-Ben, et al, Optimization of Supercontinuum Sources for Ultra-Broadband T-CARS Spectroscopy, *Chin. Phys. Lett.*, 2011, 28(3): 034202.
- [99] M Muller and J M Schins, Imaging the Thermodynamic State of Lipid Membranes with Multiplex CARS Microscopy, *J. Phys. Chem. B*, 2002, 106(14): 3715-3723.
- [100] J X Cheng, A Volkmer, L D Book and X S Xie, Multiplex Coherent Anti-Stokes Raman Scattering Microspectroscopy and Study of Lipid Vesicles, *J. Phys. Chem. B*, 2002, 106(34): 8493-8498.
- [101] T W Kee and M T Cicerone, Simple approach to one-laser, broadband coherent anti-Stokes Raman scattering microscopy, *Opt. Lett.*, 2004, 29(23): 2701-2703.
- [102] H N Paulsen, K M Hilligsoe, J Thogersen, et al, Coherent anti-Stokes Raman scattering microscopy with a photonic crystal fiber based light source, *Opt. Lett.*, 2003, 28(13): 1123-1125.
- [103] H Kano and H Hamaguchi, Femtosecond coherent anti-Stokes Raman scattering spectroscopy using supercontinuum generated from a photonic crystal fiber, *Appl. Phys. Lett.*, 2004, 85(19): 4298-4300.
- [104] A F Pegoraro, A Ridsdale, D J Moffatt, et al, Optimally chirped multimodal CARS microscopy based on a single Ti:sapphire oscillator, *Opt. Expr.*, 2009, 17(4): 2984-2996.
- [105] S O Konorov, D A Akimov, A A Ivanov, et al, Microstructure fibers as frequency-tunable sources of ultrashort chirped pulses for coherent nonlinear spectroscopy, *Appl. Phys. B.*, 2004, 78(5): 565-567.
- [106] H A Rinia, M Bonn and M Muller, Quantitative multiplex CARS spectroscopy in congested regions, *J. Phys. Chem. B.*, 2006, 110(9): 4427-4479.
- [107] Yin Jun, Yu Lingyao, Niu Hanben, et al, Theoretical Analysis of Time-resolved Coherent Anti-Stokes Raman Scattering Method for Obtaining the Whole Raman Spectrum of Biomolecules, *ACTA OPTICA SINICA*, 2010, 30 (7): 2136-2141 (in Chinese).
- [108] M Fickenscher, H G Purucker and A Laubereau, Resonant vibrational dephasing investigated by high-precision femtosecond CARS, *Chem. Phys. Lett.*, 1992, 191(1-2): 182-188.
- [109] H Okamoto, R Inaba, M Tasumi and K Yoshihara, Femtosecond vibrational dephasing of the CN stretching in alkanenitriles with long alkyl chains. Dependence on the chain length and hydrogen bonding, *Chem. Phys. Lett.*, 1993, 206(1-4): 388-392.
- [110] W Kiefer, A Materny and M Schmitt, Femtosecond time-resolved spectroscopy of elementary molecular dynamics, *Naturwissenschaften*, 2002, 89(6): 250-258.

- [111] M Schmitt, G Knopp, A Materny and W Kiefer, Femtosecond time-resolved coherent anti-Stokes Raman scattering for the simultaneous study of ultrafast ground and excited state dynamics: iodine vapour, *Chem. Phys. Lett.*, 1997, 270(1-2): 9-15.
- [112] T Joo and A C Albrecht, Femtosecond time-resolved coherent anti-Stokes Raman spectroscopy of liquid benzene: A Kubo relaxation function analysis, *J. Chem. Phys.*, 1993, 99(5): 3244-3251.
- [113] J C Kirkwood, D J Ulness and A C Albrecht, On the mechanism of vibrational dephasing in liquid benzene by coherent anti-Stokes Raman scattering using incoherent light, *Chem. Phys. Lett.*, 1998, 293(3-4): 167-172.
- [114] A Fendt, S F Fisher and W Kaiser, Vibrational lifetime and Fermi resonance in polyatomic molecules, *Chem. Phys.*, 1981, 57(1-2): 55-64.
- [115] D Pestov, M Zhi, Z E Sariyanni, et al, Femtosecond CARS of methanol-water mixtures, *J. Raman Spectrosc.*, 2006, 37(1-3): 392-396.
- [116] Y Huang, A Dogariu, Y Avitzour, et al, Discrimination of dipicolinic acid and its interferents by femtosecond coherent Raman spectroscopy, *J. Appl. Phys.*, 2006, 100(12): 124912.
- [117] M Fickenscher and A Laubereau. High-precision femtosecond CARS of simple liquids. *J. Raman Spectrosc.*, 1990, 21(12): 857-861.
- [118] G Beadie, M Bashkansky, J Reintjes and M O Scully, Towards a FAST-CARS anthrax detector: Analysis of cars generation from DPA, *J. Mod. Opt.*, 2004, 51: 2627-2635.
- [119] S Mishra, R K Singh and A K Ojha, Investigation on bonding interaction of benzonitrile with silver nano particles probed by surface enhanced Raman scattering and quantum chemical calculations, *Chem. Phys.*, 2009, 355(1): 14-20.
- [120] J X Cheng and X S Xie, Coherent Anti-Stokes Raman Scattering Microscopy: Instrumentation, Theory, and Applications, *J. Phys. Chem. B*, 2004, 108(3): 827-840.
- [121] R Inaba, K Tominaga, M Tasumi, et al, Observation of homogeneous vibrational dephasing in benzonitrile by ultrafast Raman echoes, *Chem. Phys. Lett.*, 1993, 211(2-3): 183-188.
- [122] H Okamoto, R Inaba, K Yoshihara and M Tasumi, Femtosecond time-resolved polarized coherent anti-Stokes Raman studies on reorientational relaxation in benzonitrile, *Chem. Phys. Lett.*, 1993, 202(1-2): 161-166.
- [123] Y J Lee, S H Parekh, Y H Kim and M T Cicerone, Optimized continuum from a photonic crystal fiber for broadband time-resolved coherent anti-Stokes Raman scattering, *Opt. Express*, 2010, 18(5): 4371-4379.
- [124] E Abbe, Beitræzur Theorie des Mikroskops und der mikroskopischen Wahrnehmung, *Arch. f. Mikr. Anat.*, 1873, 9(1): 413-418.
- [125] E Betzig, G H Patterson, R. Sougrat, et al., Imaging Intracellular Fluorescent Proteins at Nanometer Resolution, *Science*, 2006, 313(5793): 1642-1645.
- [126] M J Rust, M Bates and X Zhuang, Sub-diffraction-limit imaging by stochastic optical reconstruction microscopy (STORM), *Nat. Methods*, 2006, 3: 793-796.
- [127] S W Hell and J Wichmann, Breaking the diffraction resolution limit by stimulated emission: stimulated-emission-depletion fluorescence microscopy, *Opt. Lett.*, 1994, 19(11): 780-782.
- [128] S W Hell, Far-Field Optical Nanoscopy, *Science*, 2007, 316(5828): 1153-1158.
- [129] W P Beeker, P Groß, C J Lee, et al., A route to sub-diffraction-limited CARS Microscopy, *Opt. Express*, 2009, 17(25): 22632-22638.

- [130] V V Krishnamachari and E O Potma, Interferometric switching of coherent anti-Stokes Raman scattering signals in microscopy, *Phys. Rev. A*, 2009, 79(1): 013823.
- [131] K M Hajek, B Littleton, D Turk, et al., A method for achieving super-resolved widefield CARS microscopy, *Opt. Express*, 2010, 18(18): 19263-19272.
- [132] W Liu and H B Niu, Diffraction barrier breakthrough in coherent anti-Stokes Raman scattering microscopy by additional probe-beam induced phonon depletion, *Phys. Rev. A*, 2011, 83(2): 023830.

IntechOpen

IntechOpen



## **Photonic Crystals - Innovative Systems, Lasers and Waveguides**

Edited by Dr. Alessandro Massaro

ISBN 978-953-51-0416-2

Hard cover, 348 pages

**Publisher** InTech

**Published online** 30, March, 2012

**Published in print edition** March, 2012

The second volume of the book concerns the characterization approach of photonic crystals, photonic crystal lasers, photonic crystal waveguides and plasmonics including the introduction of innovative systems and materials. Photonic crystal materials promises to enable all-optical computer circuits and could also be used to make ultra low-power light sources. Researchers have studied lasers from microscopic cavities in photonic crystals that act as reflectors to intensify the collisions between photons and atoms that lead to lasing, but these lasers have been optically-pumped, meaning they are driven by other lasers. Moreover, the physical principles behind the phenomenon of slow light in photonic crystal waveguides, as well as their practical limitations, are discussed. This includes the nature of slow light propagation, its bandwidth limitation, coupling of modes and particular kind terminating photonic crystals with metal surfaces allowing to propagate in surface plasmon-polariton waves. The goal of the second volume is to provide an overview about the listed issues.

### **How to reference**

In order to correctly reference this scholarly work, feel free to copy and paste the following:

Hanben Niu and Jun Yin (2012). Ultra-Broadband Time-Resolved Coherent Anti-Stokes Raman Scattering Spectroscopy and Microscopy with Photonic Crystal Fiber Generated Supercontinuum, Photonic Crystals - Innovative Systems, Lasers and Waveguides, Dr. Alessandro Massaro (Ed.), ISBN: 978-953-51-0416-2, InTech, Available from: <http://www.intechopen.com/books/photonic-crystals-innovative-systems-lasers-and-waveguides/ultra-broadband-time-resolved-coherent-anti-stokes-raman-scattering-spectroscopy-and-microscopy-with>

**INTECH**  
open science | open minds

### **InTech Europe**

University Campus STeP Ri  
Slavka Krautzeka 83/A  
51000 Rijeka, Croatia  
Phone: +385 (51) 770 447  
Fax: +385 (51) 686 166  
[www.intechopen.com](http://www.intechopen.com)

### **InTech China**

Unit 405, Office Block, Hotel Equatorial Shanghai  
No.65, Yan An Road (West), Shanghai, 200040, China  
中国上海市延安西路65号上海国际贵都大饭店办公楼405单元  
Phone: +86-21-62489820  
Fax: +86-21-62489821

© 2012 The Author(s). Licensee IntechOpen. This is an open access article distributed under the terms of the [Creative Commons Attribution 3.0 License](#), which permits unrestricted use, distribution, and reproduction in any medium, provided the original work is properly cited.

IntechOpen

IntechOpen